

Faster Exact Exchange for Solids via occ-RI-K: Application to Combinatorially Optimized Range-Separated Hybrid Functionals for Simple Solids with Pseudopotentials Near the Basis Set Limit

Joonho Lee,^{1,*} Adam Rettig,² Xintian Feng,³ Evgeny Epifanovsky,³ and Martin Head-Gordon²

¹*Department of Chemistry, Columbia University, New York, NY, USA*

²*Department of Chemistry, University of California, Berkeley, CA, USA*

³*Q-Chem Inc., Pleasanton, CA, USA*

In this work, we developed and showcased the occ-RI-K algorithm to compute the exact exchange contribution in density functional calculations of solids near the basis set limit. Within the gaussian plane-wave (GPW) density fitting, our algorithm achieves a 1-2 orders of magnitude speedup compared to conventional GPW algorithms. Since our algorithm is well-suited for simulations with large basis sets, we applied it to 12 hybrid density functionals with pseudopotentials and a large uncontracted basis set to assess their performance on band gaps of 25 simple solids near the basis set limit. The largest calculation performed in this work involves 16 electrons and 350 basis functions in the unit cell utilizing a $6\times 6\times 6$ k-mesh. With 20-27% exact exchange, global hybrid functionals (B3LYP, PBE0, revPBE0, B97-3, SCAN0) perform similarly with a root-mean-square-deviation (RMSD) of 0.61-0.77 eV while other global hybrid functionals such as M06-2X (2.02 eV) and MN15 (1.05 eV) show higher RMSD due to their increased fraction of exact exchange. A short-range hybrid functional, HSE achieves a similar RMSD (0.76 eV) but shows a noticeable underestimation of band gaps due to the complete lack of long-range exchange. We found that two combinatorially optimized range-separated hybrid functionals, ω B97X-rV (3.94 eV) and ω B97M-rV (3.40 eV), and the two other range separated hybrid functionals, CAM-B3LYP (2.41 eV) and CAM-QTP01 (4.16 eV), significantly overestimate the band gap because of their high fraction of long-range exact exchange. Given the failure of ω B97X-rV and ω B97M-rV, we have yet to find a density functional that offers consistent performance for both molecules and solids. Our algorithm development and density functional assessment will serve as a stepping stone towards developing more accurate hybrid functionals and applying them to practical applications.

I. INTRODUCTION

Accurate predictions of band gaps (E_g) of semiconductors are often at the center of computational design of new functional materials with applications to transistors and photovoltaics.¹ Due to its computational efficiency, Kohn-Sham density functional theory (DFT) has been the workhorse for this task in modern electronic structure theory.² However, the accuracy of DFT can be quite poor for band gap problems.³ Local functionals (i.e., those functionals without exact exchange) severely underestimate band gaps³⁻⁵ whereas hybrid functionals (i.e., those with exact exchange) often overestimate band gaps.⁵⁻⁹ Beyond DFT, GW methods have been extremely successful^{10,11} but their computational cost ultimately limits their applicability to relatively small solids. Furthermore, it may suffer from ambiguity due to multiple solutions when attempting self-consistency.¹²

For main group molecular applications, there has been great progress towards finding statistically better density functionals. A high-quality database with nearly 5000 reference relative energies was used to assess 200 density functionals.² Based on that, for each rung of density functional, we have identified statistically best functionals. Combinatorially optimized density functionals (B97M-rV,^{13,14} ω B97X-rV,^{14,15} ω B97M-rV^{14,16}) developed by the Head-Gordon group clearly stood out in this benchmark study. Each of these functionals is the best-performing density functional among local den-

sity functionals, hybrid generalized gradient approximation (GGA) functionals, and hybrid meta-GGA (mGGA) functionals, respectively. Other benchmark studies have reached similar conclusions,^{17,18} including for transition-metal containing systems.^{19,20}

In our recent paper, we assessed the performance of B97M-rV and 9 other local density functionals for computing the band gaps of 37 simple semiconductors, using a large Gaussian basis set to reach the basis set limit.²¹ In that benchmark study, B97M-rV^{13,14} was found to have a root-mean-square-deviation (RMSD) of 1.18 eV and a mean-signed-error (MSD) of -0.85 eV, significantly underestimating band gaps. Nonetheless, B97M-rV and other modern mGGA functionals (SCAN,²² M06-L,²³ MN15-L²⁴) were found to be more accurate than local density approximation (LDA)^{25,26} and PBE²⁷ functionals. Motivated by this, in this work, we aim to assess the performance of modern hybrid density functionals over the same benchmark set.

Assessments of density functionals should be performed at the basis set limit as most of them were trained at this limit. The uncontracted basis set used in our previous study²¹ is fairly large and this poses computational challenges to the assessment of hybrid functionals near the basis set limit. The computational bottleneck of hybrid functionals is the evaluation of exact exchange which scales (assuming spatial locality of Gaussian basis functions) as $\tilde{O}(N_k^2 N^3)$ where N_k is the number of k-points sampled (i.e. dependent on symmetry, but not

on system size) and N denotes the size of the computational cell. In other words N represents quantities such as the number of AOs in the computational cell, n_{AO} , or the number of real-space grid points, N_g , in the cell. The cubic-scaling evaluation of exact exchange is far more expensive than the linear-scaling evaluation of the Coulomb matrix, which scales as $\mathcal{O}(N_k N)$.²¹

To cope with the steep scaling of exact exchange, we extend the occ-RI-K algorithm²⁸ developed for molecules to solids, which achieves a significant speedup compared to other algorithms when a large basis set is used. We implement this new algorithm in Q-Chem.²⁹ A similar technique known as the adaptively compressed exchange (ACE) algorithm has already been widely used in planewaves codes.³⁰ While it does not offer any scaling reduction, the occ-RI-K algorithm significantly reduces the prefactor of the exact exchange evaluation and thereby may enable extensive benchmark studies in the basis set limit such as those presented in this work. While we focus on a particular density fitting scheme, the gaussian planewave (GPW) density fitting,^{31,32} our occ-RI-K algorithm should be applicable to other periodic density fitting methods.^{33,34}

We note that efficient evaluation of exact exchange for periodic systems has seen great progress in many other available electronic structure packages. Packages such as CRYSTAL,³⁵ CP2K,³⁶ TURBOMOLE,³⁷ FHI-AIMS,³⁸ and PySCF³⁹ use Gaussian orbitals like Q-Chem. These packages often support all-electron calculations that we do not consider in this work. Nonetheless, all-electron calculations can also greatly benefit from occ-RI-K for large basis set calculations as seen in the molecular case.²⁸ Other codes based on planewaves include QuantumESPRESSO,⁴⁰ VASP,⁴¹ FLEUR,⁴² and Wien2k.⁴³ In particular, the first two employ the ACE algorithm to speed up the exact exchange calculations greatly, similar in spirit to our attempt in this work.

This paper is organized as follows: (1) we review the GPW density fitting scheme and available exact exchange algorithms, (2) we then present the occ-RI-K algorithm for solids within the GPW scheme, (3) we move to the timing benchmark of our occ-RI-K algorithm compared to other algorithms, (4) we discuss the performance of hybrid functionals on the band gap benchmark set, and (5) we then conclude.

II. THEORY

A. Review of the GPW implementation

We focus on an implementation of exact exchange within the atomic Bloch orbital framework using

$$\psi_{\mu\mathbf{k}}(\mathbf{r}) = \frac{1}{\sqrt{N_k}} \sum_{\mathbf{R}} e^{i\mathbf{k}\cdot\mathbf{R}} \phi_{\mu}(\mathbf{r} - \mathbf{R}). \quad (1)$$

where ϕ_{μ} is the μ -th atomic orbital, \mathbf{R} is the direct lattice vector, \mathbf{k} is the crystalline momentum, and $\psi_{\mu\mathbf{k}}$ is the μ -

th Bloch orbital at \mathbf{k} .

The exact exchange energy contribution to the total energy per unit cell in the atomic Bloch orbital basis is given by

$$\frac{E_K}{N_k} = -\frac{1}{2N_k} \sum_{\mathbf{k}_1, \mathbf{k}_2} \sum_{\mu\nu\lambda\sigma} P_{\mu\nu}^{\mathbf{k}_2} (\nu_{\mathbf{k}_2} \lambda_{\mathbf{k}_1} | \sigma_{\mathbf{k}_1} \mu_{\mathbf{k}_2}) P_{\lambda\sigma}^{\mathbf{k}_1} \quad (2)$$

where N_k is the number of \mathbf{k} -points, $\mathbf{P}^{\mathbf{k}}$ is the density matrix at \mathbf{k} ,

$$P_{\mu\nu}^{\mathbf{k}} = \sum_{i \in \text{occ}} C_{\mu i}^{\mathbf{k}} (C_{\nu i}^{\mathbf{k}})^* \quad (3)$$

and $(\nu_{\mathbf{k}_2} \lambda_{\mathbf{k}_1} | \sigma_{\mathbf{k}_1} \mu_{\mathbf{k}_2})$ is defined as

$$\begin{aligned} (\nu_{\mathbf{k}_2} \lambda_{\mathbf{k}_1} | \sigma_{\mathbf{k}_1} \mu_{\mathbf{k}_2}) = & \\ & \int_{\Omega^\ell} d\mathbf{r}_1 \int_{\Omega^\ell} d\mathbf{r}_2 (\psi_{\nu_{\mathbf{k}_2}}(\mathbf{r}_1))^* \psi_{\lambda_{\mathbf{k}_1}}(\mathbf{r}_1) \\ & V_{\text{coul}}(|\mathbf{r}_1 - \mathbf{r}_2|) (\psi_{\sigma_{\mathbf{k}_1}}(\mathbf{r}_2))^* \psi_{\mu_{\mathbf{k}_2}}(\mathbf{r}_2) \end{aligned} \quad (4)$$

where V_{coul} is the Coulomb operator kernel whose form depends on exchange-correlation functionals, Ω^ℓ denotes the volume of the entire simulation cell (i.e., supercell), defined as $\Omega^\ell = N_k \Omega$ with Ω being the volume of a unit cell. The Fock matrix contribution from the exchange energy is

$$K_{\nu\mu}^{\mathbf{k}_2} = \frac{\partial E_K}{\partial P_{\mu\nu}^{\mathbf{k}_2}} = - \sum_{\mathbf{k}_1} \sum_{\sigma\lambda} (\nu_{\mathbf{k}_2} \lambda_{\mathbf{k}_1} | \sigma_{\mathbf{k}_1} \mu_{\mathbf{k}_2}) P_{\lambda\sigma}^{\mathbf{k}_1} \quad (5)$$

The algorithms developed and studied in this work are based on the GPW density fitting scheme popularized by Hutter and co-workers.^{31,32} In essence, the GPW scheme expands the pair density of Bloch orbitals in terms of planewaves:

$$(\psi_{\sigma_{\mathbf{k}_1}}(\mathbf{r}))^* \psi_{\mu_{\mathbf{k}_2}}(\mathbf{r}) = \sum_{\mathbf{G}} Z_{\sigma_{\mathbf{k}_1} \mu_{\mathbf{k}_2}}^{\mathbf{G}} e^{i(\mathbf{G} - \mathbf{k}_1 + \mathbf{k}_2) \cdot \mathbf{r}} \quad (6)$$

where we evaluate the density fitting coefficients via a Fourier transform,

$$Z_{\sigma_{\mathbf{k}_1} \mu_{\mathbf{k}_2}}^{\mathbf{G}} = \frac{1}{\Omega} \int_{\Omega} d\mathbf{r} (\psi_{\sigma_{\mathbf{k}_1}}(\mathbf{r}))^* \psi_{\mu_{\mathbf{k}_2}}(\mathbf{r}) e^{-i(\mathbf{G} - \mathbf{k}_1 + \mathbf{k}_2) \cdot \mathbf{r}} \quad (7)$$

The density fitted result is then used to evaluate the Coulomb potential via an inverse Fourier transform

$$V_{\sigma_{\mathbf{k}_1} \mu_{\mathbf{k}_2}}(\mathbf{r}) = \sum_{\mathbf{G}} V_{\sigma_{\mathbf{k}_1} \mu_{\mathbf{k}_2}}^{\mathbf{G}} e^{i(\mathbf{G} - \mathbf{k}_1 + \mathbf{k}_2) \cdot \mathbf{r}} \quad (8)$$

where

$$V_{\sigma_{\mathbf{k}_1} \mu_{\mathbf{k}_2}}^{\mathbf{G}} = \begin{cases} f(|\mathbf{G} - \mathbf{k}_1 + \mathbf{k}_2|) Z_{\sigma_{\mathbf{k}_1} \mu_{\mathbf{k}_2}}^{\mathbf{G}} & \text{if } |\mathbf{G} - \mathbf{k}_1 + \mathbf{k}_2| > 0 \\ \chi & \text{if } |\mathbf{G} - \mathbf{k}_1 + \mathbf{k}_2| = 0 \end{cases} \quad (9)$$

and the form of $f(x)$ and χ depend on the underlying Coulomb operator (V_{coul}).

We consider three forms of the Coulomb operator as necessary for global hybrid, short-range hybrid, and range separated hybrid functionals, respectively:

$$f(x) = \begin{cases} \frac{4\pi}{x^2} & \text{if } V_{\text{coul}} = \frac{1}{|\mathbf{r}|} \\ \frac{4\pi}{x^2}(1 - e^{-x^2/(4\omega^2)}) & \text{if } V_{\text{coul}} = \frac{\text{erfc}(\omega|\mathbf{r}|)}{|\mathbf{r}|} \\ \frac{4\pi}{x^2}e^{-x^2/(4\omega^2)} & \text{if } V_{\text{coul}} = \frac{\text{erf}(\omega|\mathbf{r}|)}{|\mathbf{r}|} \end{cases} \quad (10)$$

χ is to correct the finite size effect and we use a simple Madelung constant correction⁴⁴ in the case of the unscreened and long-range Coulomb operators. The short-range Coulomb operator does not diverge at $x = 0$, so we use $f(x \rightarrow 0)$:

$$\chi = \frac{\pi}{\omega^2} \quad (11)$$

We also tested the truncated Coulomb operator employed by Spencer and Alavi which achieves this by combining the Coulomb and the long-range Coulomb operators:⁴⁵

$$V_{\text{coul}}(\mathbf{r}) = \begin{cases} \frac{1}{|\mathbf{r}|}\Theta(R_c - |\mathbf{r}|) \\ \frac{\text{erf}(\omega|\mathbf{r}|)}{|\mathbf{r}|}\Theta(R_c - |\mathbf{r}|) \end{cases} \quad (12)$$

where Θ is the Heaviside step function and the spherical cutoff R_c is determined from $(4\pi/3)R_c^3 = \Omega^\ell$. For range separated hybrids, we applied the truncated Coulomb operator strategy just to the long-range contribution while treating the short-range contribution exactly.⁴⁶ In reciprocal space, these transform into the following form (analogously to Eq. (10)):

$$f(x) = \frac{4\pi}{x^2}(1 - \cos(xR_c)), \quad (13)$$

for the truncated Coulomb operator and

$$f(x) = -\frac{4\pi}{x^2}\text{erf}(\omega R_c)\cos(xR_c) + \frac{2\pi}{x^2}e^{-\frac{x^2}{4\omega^2}} \times \left[\text{erf}\left(\omega\left(R_c + \frac{ix}{2\omega^2}\right)\right) + \text{erf}\left(\omega\left(R_c - \frac{ix}{2\omega^2}\right)\right) \right], \quad (14)$$

for the truncated long-range Coulomb operator.⁴⁶ Both cases have well-defined $x \rightarrow 0$ limits and therefore one can use $\chi = f(x \rightarrow 0)$. The erf terms in Eq. (14) diverge as $x \rightarrow \infty$ and the multiplicative exponential function decays to zero as $x \rightarrow \infty$. These two terms cancel each other and produce a finite, well-behaved quantity in the end but some care is needed for a numerically stable evaluation as described in Appendix A1.

In GPW, the Fourier transforms are handled by the discrete Fourier transform as implemented in fast Fourier transform libraries. The computational complexity of each Fourier transform call is $\mathcal{O}(N_g \log N_g)$ where N_g is the number of grid points used in the unit cell. Using the GPW density fitting, we consider a total of three algorithms in this work where all three yield exactly the same ground state energy and valence band (occupied orbital) energies. While some of our algorithms are capable of avoiding the storage of $\psi_{\mu\mathbf{k}}(\mathbf{r})$ on the real-space grid, for the descriptions below we assume that this tensor can be stored in memory. We describe a strategy to avoid storing $\psi_{\mu\mathbf{k}}(\mathbf{r})$ within the occ-RI-K algorithm in Section II E.

B. Atomic Orbital (AO)-RI-K algorithm

In the AO-RI-K algorithm, our goal is to compute Eq. (5) as written and a pair of Bloch atomic orbitals as shown in Eq. (6) is density fitted. A nice feature of this algorithm is that one can benefit from exploiting the sparse structure of Bloch atomic orbitals ($\{\psi_{\mu\mathbf{k}}\}$) where we can assume that only a small number of grid points carry non-zero values for each Bloch atomic orbital. Our scaling analysis will assume this as our implementation exploits this.

The AO-RI-K algorithm (shown in Algorithm 1) starts by forming the following intermediate:

$$\tilde{\psi}_{\sigma\mathbf{k}_1}(\mathbf{r}) = \sum_{\lambda} P_{\lambda\sigma}^{\mathbf{k}_1} \psi_{\lambda\mathbf{k}_1}(\mathbf{r}) \quad (15)$$

which costs $\mathcal{O}(N_k N_g)$ memory and $\mathcal{O}(N_k N_g n_{\text{AO}})$ compute where sparsity was used to remove the scaling with n_{AO} . Looping over pairs of k-points (\mathbf{k}_1 and \mathbf{k}_2) and pairs of atomic orbital indices ($\mu_{\mathbf{k}_2}$, $\sigma_{\mathbf{k}_1}$), we evaluate Eq. (8) with $\mathcal{O}(N_k^2 n_{\text{AO}}^2 N_g \log N_g)$ (i.e. cubic) effort, where n_{AO} is the number of atomic Bloch orbitals in the unit cell. Within the inner loops over \mathbf{k}_1 and $\sigma_{\mathbf{k}_1}$, we accumulate the following intermediate (starting from zero),

$$\tilde{V}_{\mu\mathbf{k}_2}(\mathbf{r}) = \sum_{\mathbf{k}_1} \sum_{\sigma_{\mathbf{k}_1}} \tilde{\psi}_{\sigma_{\mathbf{k}_1}}(\mathbf{r}) V_{\sigma_{\mathbf{k}_1} \mu_{\mathbf{k}_2}}(\mathbf{r}) \quad (16)$$

which scales as $\mathcal{O}(N_k^2 n_{\text{AO}}^2 N_g)$ and we accumulate the final exchange matrix contribution,

$$K_{\nu\mu}^{\mathbf{k}_2} = - \sum_{\mathbf{r}} \tilde{V}_{\mu\mathbf{k}_2}(\mathbf{r}) (\psi_{\nu\mathbf{k}_2}(\mathbf{r}))^* \quad (17)$$

which scales as $\mathcal{O}(N_k N_g)$ after sparsity was used to remove the dependence of the scaling on n_{AO} . The bottleneck of this algorithm is executing the FFT, which scales as $\mathcal{O}(N_k^2 n_{\text{AO}}^2 N_g \log N_g)$.

Algorithm 1: AO-RI-K algorithm.

```

Perform Eq. (15). //  $\mathcal{O}(N_k N_g)$ 
for  $\mathbf{k}_2 = 1$  to  $N_k$  do // Parallel loop.
for  $\mu_{\mathbf{k}_2} = 1$  to  $n_{\text{AO}}$  do // Parallel loop.
for  $\mathbf{k}_1 = 1$  to  $N_k$  do
for  $\sigma_{\mathbf{k}_1} = 1$  to  $n_{\text{AO}}$  do
Form Eq. (8). //  $\mathcal{O}(N_k^2 n_{\text{AO}}^2 N_g \log N_g)$ 
Execute Eq. (16) to obtain  $\tilde{V}$ . //  $\mathcal{O}(N_k^2 n_{\text{AO}}^2 N_g)$ 
end
end
Execute Eq. (17). //  $\mathcal{O}(N_k N_g)$ 
end
end

```

C. Molecular Orbital (MO)-RI algorithm

In the MO-RI algorithm,^{47–49} we compute the exchange matrix via

$$K_{\nu\mu}^{\mathbf{k}_2} = - \sum_{\mathbf{k}_1} \sum_{i \in \text{occ}} (\nu_{\mathbf{k}_2} i_{\mathbf{k}_1} | i_{\mathbf{k}_1} \mu_{\mathbf{k}_2}) \quad (18)$$

where an occupied orbital is defined as

$$\psi_{i_{\mathbf{k}}}(\mathbf{r}) = \sum_{\mu} C_{\mu i}^{\mathbf{k}} \psi_{\mu_{\mathbf{k}}}(\mathbf{r}) \quad (19)$$

We form this intermediate at the cost of $\mathcal{O}(N_k N_g n_{\text{occ}})$ (with sparsity) operations, where n_{occ} is the number of occupied orbitals and store this in memory. This $N_k N_g n_{\text{occ}}$ memory requirement scales quadratically with cell size.

In the MO-RI algorithm, we density fit the $(\psi_{i_{\mathbf{k}_1}}(\mathbf{r}))^* \psi_{\mu_{\mathbf{k}_2}}(\mathbf{r})$ products. Looping over pairs of k-points, occupied orbital indices, and atomic orbital indices, the overall cubic cost of density fitting will scale as $\mathcal{O}(N_k^2 n_{\text{occ}} n_{\text{AO}} N_g \log N_g)$. This suggests an immediate cost reduction from AO-RI to MO-RI is obtained by a factor of $n_{\text{AO}}/n_{\text{occ}}$, which can be a significant speedup when one considers a relatively large (such as triple-zeta or larger) basis set. This speedup can be roughly a factor of 5 for triple-zeta quality bases and becomes larger as the basis set size is increased (keeping the system size fixed).

Algorithm 2: MO-RI-K algorithm.

```

Perform Eq. (19). //  $\mathcal{O}(N_k N_g n_{\text{occ}})$ 
for  $\mathbf{k}_2 = 1$  to  $N_k$  do // Parallel loop.
  for  $\mu_{\mathbf{k}_2} = 1$  to  $n_{\text{AO}}$  do // Parallel loop.
    for  $\mathbf{k}_1 = 1$  to  $N_k$  do
      for  $i_{\mathbf{k}_1} = 1$  to  $n_{\text{occ}}$  do
        Form  $V_{i_{\mathbf{k}_1} \mu_{\mathbf{k}_2}}(\mathbf{r})$ . //  $\mathcal{O}(N_k^2 n_{\text{AO}} n_{\text{occ}} N_g \log N_g)$ 
        Execute Eq. (20) to obtain  $W$ . //  $\mathcal{O}(N_k^2 n_{\text{AO}} n_{\text{occ}} N_g)$ 
      end
    end
  Execute Eq. (17) with  $W$ . //  $\mathcal{O}(N_k N_g)$ 
end
end

```

The overall MO-RI algorithm, summarized in Algorithm 2, is similar to the AO-RI algorithm. One loops over a pair of k-points $(\mathbf{k}_1, \mathbf{k}_2)$, occupied orbital indices $i_{\mathbf{k}_1}$, and atomic orbital indices $\mu_{\mathbf{k}_2}$ and forms the Coulomb potential $V_{i_{\mathbf{k}_1} \mu_{\mathbf{k}_2}}(\mathbf{r})$ that arises from the density, $(\psi_{i_{\mathbf{k}_1}}(\mathbf{r}))^* \psi_{\mu_{\mathbf{k}_2}}(\mathbf{r})$. One then accumulates the following intermediate in the inner loop (i.e. the loops over \mathbf{k}_1 and $i_{\mathbf{k}_1}$):

$$W_{\mu_{\mathbf{k}_2}}(\mathbf{r}) = \sum_{\mathbf{k}_1} \sum_{i_{\mathbf{k}_1}} \psi_{i_{\mathbf{k}_1}}(\mathbf{r}) V_{i_{\mathbf{k}_1} \mu_{\mathbf{k}_2}}(\mathbf{r}) \quad (20)$$

with compute cost scaling as $\mathcal{O}(N_k^2 n_{\text{AO}} n_{\text{occ}} N_g)$. The K-matrix accumulation is done the same way as Eq. (17)

with the intermediate in Eq. (20) in the outer loop with the same cost of $\mathcal{O}(N_k n_{\text{AO}}^2)$. Similar to the AO-RI algorithm, the FFT calls were found to be the bottleneck, with cubic scaling compute cost of $\mathcal{O}(N_k^2 n_{\text{AO}} n_{\text{occ}} N_g \log N_g)$.

D. Occupied orbital (occ)-RI-K algorithm

The occ-RI-K algorithm²⁸ speeds up evaluation of the exact exchange operator by *ignoring* its component in the virtual space. In other words, denoting the occupied orbital space projector as \hat{P} and the unoccupied orbital space projector as \hat{Q} , one can approximate

$$\hat{K} \simeq \hat{P} \hat{K} \hat{P} + \hat{P} \hat{K} \hat{Q} + \hat{Q} \hat{K} \hat{P} \quad (21)$$

ignoring $\hat{Q} \hat{K} \hat{Q}$. This approximation is *exact* when considering quantities that depend only on occupied orbitals such as the self-consistent field (SCF) energy, the valence band energies and orbitals, and of course the density matrix.

Using the same idea, we will compute only part of the exchange matrix,

$$K_{\nu j}^{\mathbf{k}_2} = - \sum_{\mathbf{k}_1} \sum_{i \in \text{occ}} (\nu_{\mathbf{k}_2} i_{\mathbf{k}_1} | i_{\mathbf{k}_1} j_{\mathbf{k}_2}) \quad (22)$$

to obtain the AO-occupied block of \mathbf{K} . This amounts to the computation of $(\hat{P} + \hat{Q}) \hat{K} \hat{P}$ which can be used to obtain Eq. (21) with simple matrix multiplications for each k-point.²⁸ Since the computational bottleneck of AO-RI-K and MO-RI-K is the FFT step, our goal is to reduce the prefactor for this step using the same intuition as occ-RI-K.

In the occ-RI-K algorithm, shown in Algorithm 3, one first forms the intermediates in Eq. (19) and loops over a pair of k-points $(\mathbf{k}_1, \mathbf{k}_2)$ and a pair of occupied orbitals $(i_{\mathbf{k}_1}, j_{\mathbf{k}_2})$. The density, $(\psi_{i_{\mathbf{k}_1}}(\mathbf{r}))^* \psi_{j_{\mathbf{k}_2}}(\mathbf{r})$, will be fitted by planewaves and the corresponding Coulomb potential, $V_{i_{\mathbf{k}_1} j_{\mathbf{k}_2}}(\mathbf{r})$ is formed at $\mathcal{O}(N_k^2 n_{\text{occ}}^2 N_g \log N_g)$ cost. Similarly to the other GPW algorithms, in the inner loops $(\mathbf{k}_1, i_{\mathbf{k}_1})$ one accumulates the following intermediate:

$$\tilde{W}_{j_{\mathbf{k}_2}}(\mathbf{r}) = \sum_{\mathbf{k}_1} \sum_{i_{\mathbf{k}_1}} \psi_{i_{\mathbf{k}_1}}(\mathbf{r}) V_{i_{\mathbf{k}_1} j_{\mathbf{k}_2}}(\mathbf{r}) \quad (23)$$

with $\mathcal{O}(N_k^2 n_{\text{occ}}^2 N_g)$ compute cost. We assume that we have enough memory to hold $\tilde{W}(\mathbf{r})$, imposing an $\mathcal{O}(N_k n_{\text{occ}} N_g)$ quadratic-scaling storage requirement (significantly smaller than required to hold $\psi_{\nu_{\mathbf{k}_2}}(\mathbf{r})$). After obtaining \tilde{W} , we compute

$$K_{\nu j}^{\mathbf{k}_2} = - \sum_{\mathbf{r}} \tilde{W}_{j_{\mathbf{k}_2}}(\mathbf{r}) (\psi_{\nu_{\mathbf{k}_2}}(\mathbf{r}))^* \quad (24)$$

at $\mathcal{O}(N_k n_{\text{occ}} N_g)$ cost, assuming sparsity of $\psi_{\nu_{\mathbf{k}_2}}(\mathbf{r})$. Compared to the MO-RI-K algorithm, we achieve a clear

$n_{\text{AO}}/n_{\text{occ}}$ speed-up in all steps in the loop. Most importantly, the number of FFT calls is reduced from $N_k^2 n_{\text{AO}} n_{\text{occ}}$ to $N_k^2 n_{\text{occ}}^2$.

Algorithm 3: occ-RI-K algorithm.

```

Perform Eq. (19). //  $\mathcal{O}(N_k N_g n_{\text{occ}})$ 
for  $\mathbf{k}_2 = 1$  to  $N_k$  do // Parallel loop.
for  $j_{\mathbf{k}_2} = 1$  to  $n_{\text{occ}}$  do // Parallel loop.
for  $\mathbf{k}_1 = 1$  to  $N_k$  do // Parallel loop.
for  $i_{\mathbf{k}_1} = 1$  to  $n_{\text{occ}}$  do // Parallel loop.
Form  $V_{i_{\mathbf{k}_1} j_{\mathbf{k}_2}}(\mathbf{r})$ . //  $\mathcal{O}(N_k^2 n_{\text{occ}}^2 N_g \log N_g)$ 
Execute Eq. (23) to obtain  $\tilde{W}$ . //  $\mathcal{O}(N_k^2 n_{\text{occ}}^2 N_g)$ 
end
end
end
end
Execute Eq. (24). //  $\mathcal{O}(N_k N_g n_{\text{occ}})$ 

```

In some applications, one may want to compute the first few conduction bands (unoccupied orbitals). This is particularly important when one tries to compute the band gap. In that case, one can simply extend the occ-RI-K algorithm to compute the first few conduction bands *exactly*. We write $\hat{Q} = \hat{R} + \hat{S}$ where \hat{R} is the projector onto the space spanned by conduction bands of our interest and \hat{S} is the projector onto the rest of the conduction bands. Then, we can approximate \hat{K} by

$$\hat{K} \simeq \hat{P}\hat{K}\hat{P} + \hat{P}\hat{K}\hat{Q} + \hat{Q}\hat{K}\hat{P} + \hat{R}\hat{K}\hat{R} + \hat{R}\hat{K}\hat{Q} + \hat{Q}\hat{K}\hat{R} \quad (25)$$

This only needs the evaluation of $K_{vp}^{\mathbf{k}_2}$ where p includes valence bands (occupied orbitals) and desired conduction bands (unoccupied orbitals) at \mathbf{k}_2 . However, when $\{\mathbf{k}_1\}$ (i.e., those used for the ground state calculations) and $\{\mathbf{k}_2\}$ (those used for the band calculations) in Eq. (24) are different, the occ-RI-K algorithm described above is no longer applicable because one does not have orbitals available for $\{\mathbf{k}_2\}$. As a workaround, one may append $\{\mathbf{k}_1\}$ with $\{\mathbf{k}_2\}$ for the ground state calculations or employ Wannier interpolation⁵⁰ to obtain orbitals at $\{\mathbf{k}_2\}$ from orbitals at $\{\mathbf{k}_1\}$.

E. Integral-direct strategies

The memory requirement for storing the basis function on grid points ($\psi_{\mu_{\mathbf{k}}}(\mathbf{r})$) scales as $\mathcal{O}(N_g N_k)$ assuming the sparsity of the underlying basis functions. In practice, the sparsity may not be effective with a relatively tight threshold until we reach a very large computational cell. In such cases, the required memory can scale as $\mathcal{O}(N_g N_k n_{\text{AO}})$ which can be quite sizable. If this memory consumption is unaffordable, one needs to resort to an “integral-direct” strategy where one does not store $\psi_{\mu_{\mathbf{k}}}(\mathbf{r})$ in memory, but instead computes them on-the-fly.

This leads to a small modification of Algorithm 3 as shown in Algorithm 4. The only difference is that one repeatedly computes $\psi_{i_{\mathbf{k}}}(\mathbf{r})$ adding an extra computational cost of $\mathcal{O}(N_k^2 N_g n_{\text{occ}}^2)$. This step is not more expensive than other parts of the algorithm. In our implementation, depending on available memory, the integral-direct algorithm is triggered. A similar strategy has been explored in Gaussian density fitting recently.⁵¹

Algorithm 4: Integral-direct occ-RI-K algorithm.

```

for  $\mathbf{k}_2 = 1$  to  $N_k$  do
for  $j_{\mathbf{k}_2} = 1$  to  $n_{\text{occ}}$  do // Parallel loop.
for  $\mathbf{k}_1 = 1$  to  $N_k$  do // Parallel loop.
for  $i_{\mathbf{k}_1} = 1$  to  $n_{\text{occ}}$  do // Parallel loop.
Perform Eq. (19) for  $i_{\mathbf{k}_1}, j_{\mathbf{k}_2}$ . //  $\mathcal{O}(N_k^2 N_g n_{\text{occ}}^2)$ 
Form  $V_{i_{\mathbf{k}_1} j_{\mathbf{k}_2}}(\mathbf{r})$ . //  $\mathcal{O}(N_k^2 n_{\text{occ}}^2 N_g \log N_g)$ 
Execute Eq. (23) to obtain  $\tilde{W}$ . //  $\mathcal{O}(N_k^2 n_{\text{occ}}^2 N_g)$ 
end
end
Execute Eq. (24) for  $j_{\mathbf{k}_2}$ . //  $\mathcal{O}(N_k N_g n_{\text{occ}})$ 
end
end

```

III. COMPUTATIONAL DETAILS

Functional	Year	Hybrid type	Ingredients	$c_{x, sr}$	$c_{x, lr}$
B3LYP ⁵²	1993	GH	GGA	0.20	
PBE0 ⁵³	1996	GH	GGA	0.25	
revPBE0 ⁵⁴	1998	GH	GGA	0.25	
B97-3 ⁵⁵	2005	GH	GGA	0.269288	
M06-2X ⁵⁶	2008	GH	mGGA	0.54	
MN15 ⁵⁷	2016	GH	mGGA	0.44	
SCAN0 ⁵⁸	2016	GH	mGGA	0.25	
HSE ⁵⁹⁻⁶²	2008	RSH	GGA	0.25	0.00
CAM-B3LYP ⁶³	2004	RSH	GGA	0.19	0.65
ω B97X-rV ¹⁵	2014	RSH	GGA	0.167	1.00
ω B97M-rV ¹⁶	2016	RSH	mGGA	0.15	1.00
CAM-QTP01 ⁶⁴	2016	RSH	GGA	0.23	1.00

TABLE I: Summary of 12 density functionals investigated in this work. $c_{x, sr}$ is the coefficient for the short-range exact exchange and $c_{x, lr}$ is the coefficient for the long-range exact exchange.

We consider a total of 12 density functionals in this work. There are seven global hybrid (GH) functionals and four range separated hybrid (RSH) functionals, with a range of different amount of exact exchange and year of development. For GGA GH functionals, B3LYP,⁵² PBE0,⁵³ revPBE0,⁵⁴ and B97-3⁵⁵ were considered. For mGGA GH functionals, M06-2X,⁵⁶ MN15,⁵⁷ and SCAN0⁵⁸ were considered. For RSH functionals, we consider a short-range functional (HSE⁵⁹⁻⁶²) and four long-range corrected density functionals (CAM-B3LYP,⁶³ ω B97X-rV,¹⁵ ω B97M-rV,¹⁶ CAM-QTP01⁶⁴).

We do not consider dispersion corrections such as D2, D3, and D3(BJ)^{65–67} in this work because they do not affect the band gaps at all. In practical applications besides the band gap, all of the aforementioned functionals, except ω B97X-rV and ω B97M-rV, should be supplemented by dispersion corrections. All our calculations were performed with a development version of Q-Chem.²⁹ For relatively well studied functionals, PBE0 and HSE, we compare our band gaps against literature values in Refs. 9,68 and found an excellent agreement (see Fig. AI).

We summarize these functionals in Table I along with their fraction of short-range ($c_{x,\text{sr}}$) and long-range ($c_{x,\text{lr}}$) exact exchange. One key feature of ω B97X-rV, ω B97M-rV, and CAM-QTP01 is that they include the long-range exact exchange contribution up to 100%. Intuitively, this can be worrisome for band gap applications because in the long-range there is no Coulomb screening present in the method (like in Hartree-Fock theory). Another interesting remark about CAM-QTP01 is that this is an RSH functional fitted to experimental ionization potentials, which may be a useful property for improving the band gaps.⁶⁴ We will see how these manifest in the band gap benchmark later.

We used a large uncontracted basis set developed in our previous paper (unc-def2-QZVP-GTH)²¹ to ensure that we obtain band gaps near the basis set limit. We used the GTH-PBE pseudopotential for all functionals considered in this work due to the lack of functional-specific GTH pseudopotentials for these functionals.^{69,70} We took the geometry and experimental band gaps of 25 solids from ref. 21 (also see references therein).

As it was tested for local functionals,²¹ the band gap change due to the pseudopotential is expected to be much smaller than the band gap error energy scale that we will discuss here. We used $6 \times 6 \times 6$ Monkhorst-Pack \mathbf{k} -mesh which is sufficient to reach the thermodynamic limit for systems discussed in this work. For our GPW calculations, we followed the same E_{cut} value as our previous study.²¹ Namely, we used E_{cut} of 1500 eV for every solid considered in this work. To measure the remaining basis set incompleteness error, we compared the Γ -point band gap of B3LYP computed by our code against those from QuantumESPRESSO.⁴⁰ We used a kinetic energy cut-off of 400 Ry for every system. The basis set error of our band gap calculations with GTOs is smaller than 10 meV, which is consistent with what we found for local density functionals.²¹ This comparison is available in Table AIV. We also compare the total energy in Table AIII and confirm that the basis set error in total energy with a $6 \times 6 \times 6$ \mathbf{k} -mesh is less than $0.5 \text{ m}E_h$ per cell.

We used finite size correction strategies described in Section II A for handling the divergence of exact exchange term. For the ground state SCF calculations, we used the simple Madelung constant correction.⁴⁴ While this correction scheme smoothly converged the ground state SCF energies to the thermodynamic limit up to the \mathbf{k} -mesh of $6 \times 6 \times 6$, the subsequent band structure calculations showed erratic discontinuities in the resulting bands. We

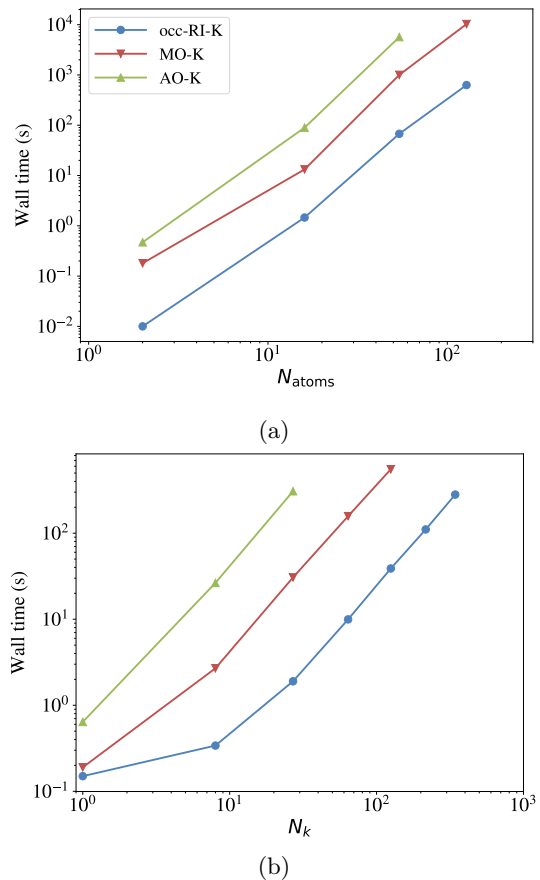


FIG. 1: Wall time (seconds) of a single exchange-matrix build for the three exchange algorithms presented for diamond (a) Γ -point calculations as a function of the number of atoms in the super cell and (b) \mathbf{k} -point calculations as a function of the number of \mathbf{k} -points. Given the same total number of C atoms, all methods in (a) and (b) yield the same total energy per C atom.

confirmed that this is due to the residual size effect so we switched to the truncated Coulomb operator technique⁴⁵ when computing bands. Nonetheless, the band gaps using two different correction schemes are in a qualitative agreement as can be seen in Table AI and Table AII.

The largest calculation that we performed in this work involves up to 350 basis functions and 16 electrons in the central unit cell (i.e., AlN) with $6 \times 6 \times 6$ \mathbf{k} -mesh.

IV. RESULTS AND DISCUSSION

A. Timing benchmark

We benchmarked the compute time of each exact exchange algorithm on a single test case, diamond with QZV2P-GTH basis set.⁷¹ Diamond is chosen because it is a representative semiconductor, and QZV2P-GTH is employed so that the benefit of occ-RI-K can be high-

lighted. We tested the scaling with respect to system size as well as number of k -points. All calculations were done on 32 cores using two AMD Opteron 6376 processors.

In Table II and Table III, we present the Hartree-Fock total energies per atom of diamond with varying supercell size (Table II) and k -mesh (Table III). Comparing the two tables, we illustrate the equivalence of the supercell and k -point implementations for the same number of atoms. Furthermore, we show that our occ-RI-K implementation makes no additional approximations beyond AO-K and MO-K as emphasized in Section IID. AO-K, MO-K, and occ-RI-K energies agree with each other for the same number of atoms.

We analyzed the scaling with respect to system size via supercell Γ -point calculations. Fig. 1a shows the wall time of each exchange algorithm as a function of the number of atoms included in the supercell. We see that AO-K quickly becomes intractable for large systems; a $3\times 3\times 3$ supercell, corresponding to 54 atoms per unit cell in the calculation, is about the limit of this algorithm for the diamond system. The MO-K algorithm is over five times faster for all supercells considered. This allows calculations with two to three times the number of electrons as the AO-K algorithm. Finally, the occ-RI-K algorithm provides an additional speedup over MO-K of almost 15 for most supercells considered, allowing even larger calculations. Overall, occ-RI-K achieves nearly two orders of magnitude speedup compared to the AO-K algorithm. Furthermore, the slope of occ-RI-K in the log-log plot in Fig. 1a suggests that the algorithm scales as $\mathcal{O}(N^{2.9})$ which confirms the cubic-scaling with respect to system size as noted in Section IID.

We additionally analyzed the performance of each algorithm where we fix the size of the unit cell (two carbon atoms per cell) and vary the number of k -points. For these we find that MO-K offers roughly a factor of 10 speedup over AO-K and occ-RI-K further speeds this up by an additional factor of roughly 15. The speedup provided by occ-RI-K is more than two orders of magnitude speedup compared to the AO-K algorithm. The slope of occ-RI-K algorithm in Fig. 1b confirms $\mathcal{O}(N_k^{2.0})$ scaling consistent with our scaling analysis presented in Section IID. We note that calculations with small k -meshes as well as small supercells can be unphysical in that the finite size error can be substantial. We, nonetheless, performed these calculations to analyze computational scaling.

While more practical application of exact exchange will likely be much more difficult than our prototypical example, diamond, we see that occ-RI-K offers substantial speedups over alternatives, allowing calculations with significantly more electrons and k -points.

We also performed a set of timing benchmark calculations of diamond and AlN with a $6\times 6\times 6$ k -mesh as a function of the basis set size (SZV-GTH, DZVP-GTH, TZV2P-GTH, QZV2P-GTH, unc-def2-QZVP-GTH.) In Fig. 2, the corresponding timing results are presented.

N_{atoms}	Supercell		
	AO-K	MO-K	occ-RI-K
2	-5.1913973	-5.1913973	-5.1913973
16	-5.5159556	-5.5159556	-5.5159556
54	N/A	-5.5436244	-5.5436244

TABLE II: Hartree-Fock total energies per atom (E_h) using the Γ -point implementation for various supercell sizes. N/A means not available.

N_{atoms}	k -point		
	AO-K	MO-K	occ-RI-K
2	-5.1913973	-5.1913973	-5.1913973
16	-5.5159556	-5.5159556	-5.5159556
54	-5.5436244	-5.5436244	-5.5436244
128	N/A	-5.5460132	-5.5460132
250	N/A	-5.5456075	-5.5456075
432	N/A	N/A	-5.5450982
686	N/A	N/A	-5.5447456

TABLE III: Hartree-Fock total energies per atom (E_h) using the k -point implementation for various k -mesh sizes (i.e., the number of atoms). N/A means not available.

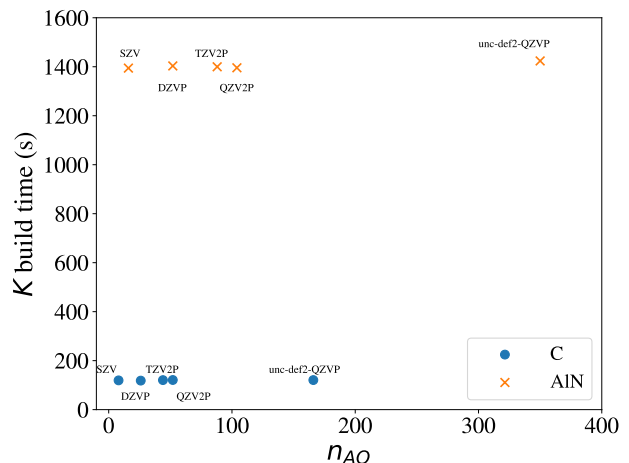


FIG. 2: Wall time (seconds) of a single K-matrix build with varying basis set sizes. AlN and C have 16 and 8 electrons in the unit cell, respectively.

We observe nearly no basis set size dependence in our K-matrix build time due to the fact that the number of expensive FFT calls is independent of the number of basis functions. This highlights the utility of occ-RI-K even further.

B. Band gap assessment

We first discuss the overall band gap distribution of each functional as shown in Fig. 3. Along the dotted line of $y = x$, we observe that round and triangle data points are relatively well aligned. These are GGA GH

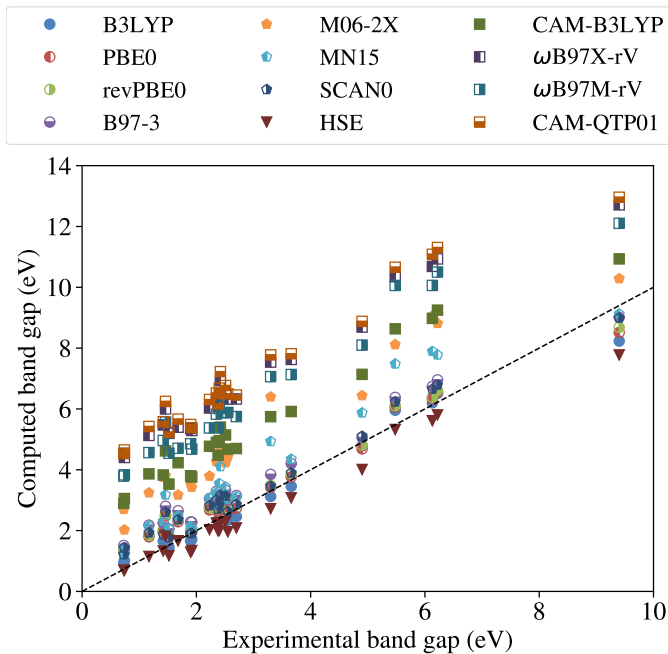


FIG. 3: Scatter plot of computed band gap (eV) versus experimental band gap (eV). Round markers are used for GGA global hybrids, pentagons are used for mGGA global hybrids, triangles are used for short-range hybrid functional (HSE), and squares are used for long-range corrected range separated functionals. The black dotted line is guide for the eye.

functionals and HSE, respectively. It is widely accepted that HSE performs well for band gap problems, but the good performance of GGA GH functionals is not so well-known.^{9,68} However, some deterioration of the good performance of both these classes of functionals is noticeable in Fig. 3 for larger band gap materials (above 6 eV).

Given they are more recently developed functionals, mGGA GH functionals (pentagons) are quite disappointing. M06-2X and MN15 have a high fraction of exact exchange ($\sim 50\%$). This higher fraction of exact exchange compared to other GGA GHs (all about $\sim 25\%$) seems to be the cause for an overall overestimation of the band gaps. With 25% of exact exchange, SCAN0 performs better than M06-2X and MN15, but it still seems slightly worse than GGA GHs.

Lastly, the performance of long-range corrected functionals (squares) is catastrophic with the tendency of overestimating band gaps for all materials considered here. The short-range exact exchange is only 15%–20% in these functionals, which is even less than HSE (25%). This gross overestimation of band gaps is likely due to the large fraction of long-range exact exchange. CAM-B3LYP has 65% of long-range exact exchange while both of the combinatorially optimized functionals and CAM-QTP01 have 100% long-range exact exchange.

We obtain a more global perspective by inspecting the statistical data presented in Fig. 4. In terms

of root-mean-square-deviation (RMSD), B3LYP, PBE0, revPBE0, B97-3, SCAN0, and HSE are all quite comparable (0.61–0.77 eV). Other functionals including MN15, M06-2X, CAM-B3LYP, ω B97X-rV, ω B97M-rV, and CAM-QTP01 are significantly worse than these functionals. The worst performing functional is CAM-QTP01 (4.16 eV) and the second worst performing functional is ω B97X-rV (3.94 eV). In terms of mean-average-deviation (MAD), another interesting trend arises. The HSE functional has a noticeable, negative MAD, which is likely due to the lack of long-range exact exchange. Other functionals with a higher fraction of exact exchange show positive MAD values. Given these data, following the combinatorial design strategy, it may be beneficial to develop a variant of ω B97X-rV or ω B97M-rV where the long-range exact exchange is limited to less than 25%. Examining the difference between maximum deviation and minimum deviation, we found more modern functionals such as M06-2X (2.54 eV) may benefit more from error cancellation in practice than B3LYP (3.78 eV). The raw data for plots presented here are available in Table AII.

C. Outlook for future functional developments

To gain more insights into functional developments, we examine the effect of the fraction of long-range exact exchange (i.e., $c_{x,lr}$) in ω B97M-rV on five solids (Ge, Si, SiC, C, LiF), whose experimental band gaps range from 0.74 eV to 14.2 eV. These results are presented in Fig. 5. Despite the fact that we relaxed orbitals for each of $c_{x,lr}$ values, the change in band gaps shows a completely linear behavior with respect to $c_{x,lr}$. This is observed in nearly all bands (Fig. 6), not just in the frontier bands. The band structure shows a nearly constant shift for different $c_{x,lr}$ values.

The most striking aspect of this plot is that the optimal $c_{x,lr}$ for four solids (Ge, Si, SiC, and C) is around 0.25–0.3 whereas the optimal value for LiF is near 0.75. $c_{x,lr}$ of 0.25–0.3 is close to the fraction of exact exchange in the GH functionals that perform well as discussed in Section IV B. Qualitatively, large gap materials do not benefit as much from screening and rather more long-range exact exchange is desirable. This is qualitatively similar to what we see from molecular systems that typically exhibit large gaps. This has been previously pointed out several others in literature.^{9,72–74}

Given these observations, there are two potential ways for future functional developments that can perform well for both solids and molecules. The first is that one may combinatorially optimize a density functional with short-range, middle-range, and long-range exact exchange.^{75–77} The idea is that one should not have a too high fraction of long-range exact exchange for small-to-medium-gap materials, but one would need a large fraction of middle-range exact exchange for good performance on large-gap materials and molecules. The second idea is to develop a system-specific density functional that would

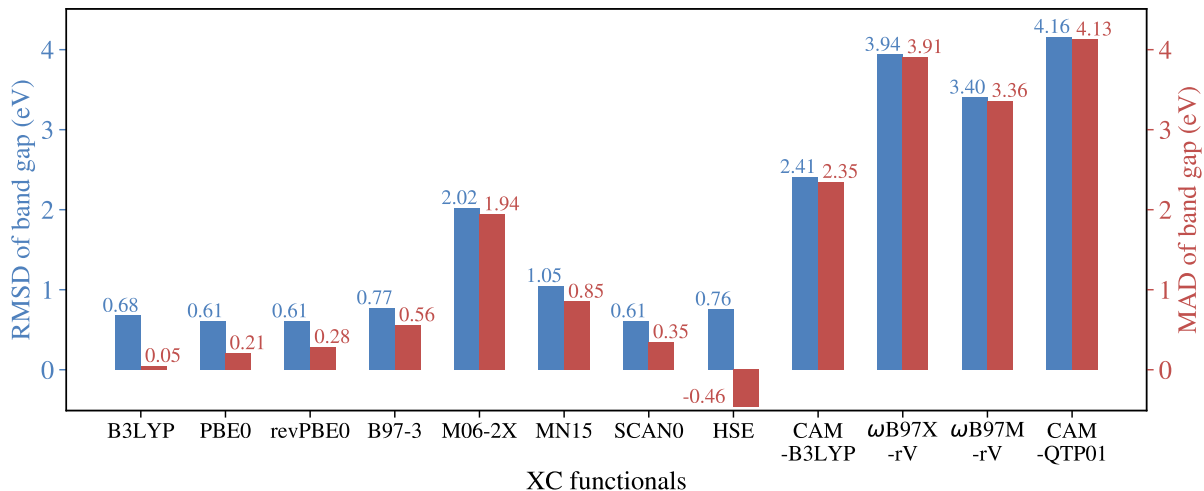


FIG. 4: Band gap (eV) comparison over 25 solids between DFT (12 different functionals) and experiments: Blue: root-mean-square-deviation (RMSD) of DFT band gaps (eV) with respect to those of experiments and Red: mean-average-deviation (MAD) of DFT band gaps (eV) with respect to those of experiments.

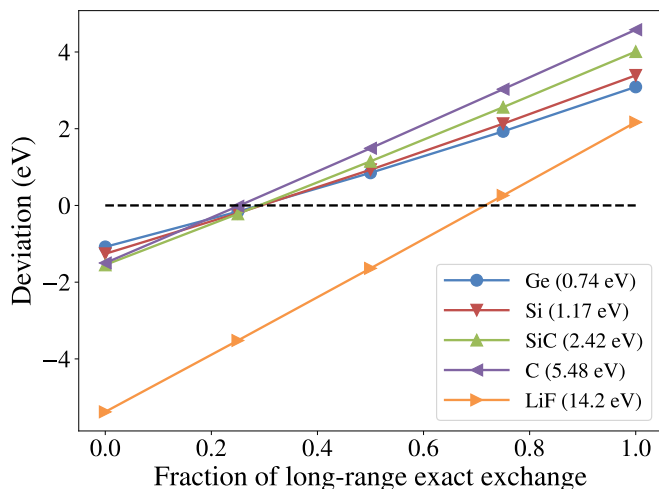


FIG. 5: Deviation (eV) of the computed band gaps from ω B97M-rV with respect to experimental band gaps (given in parentheses) as a function of the fraction of long-range exact exchange ($c_{x,lr}$).

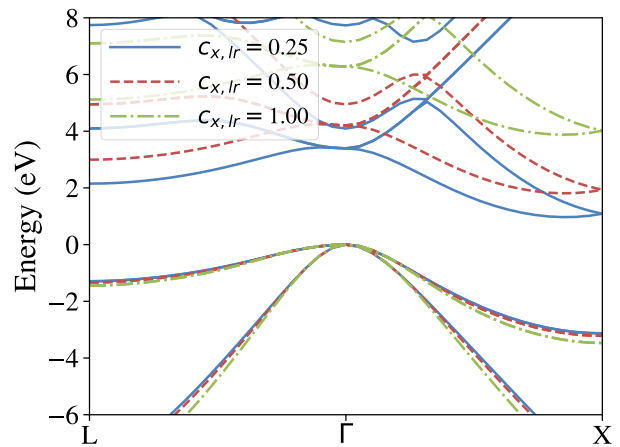


FIG. 6: Bands of Si computed from ω B97M-rV as a function of the fraction of long-range exact exchange ($c_{x,lr}$). The Γ -point valence band maximum is shifted to zero for comparisons.

V. CONCLUSIONS

vary the fraction of exact exchange depending on the system. This is closely related to the dielectric-dependent hybrid functionals developed by Galli and co-workers,⁷⁴ but its performance on molecular systems has not been extensively assessed yet.⁷⁸ The last is to minimize the quasiparticle energy correction from G0W0 by tuning the fraction of exact exchange following the work by Atalla *et al.*^{79–81} This approach has shown promising accuracy for molecules and solids.

In this work, the occ-RI-K algorithm²⁸, which was originally developed for and has been successfully applied to molecules, has been extended to evaluate exact exchange in solid-state applications. Within the GPW density fitting scheme,^{31,32} we showed that the occ-RI-K algorithm achieves a nearly 1-2 orders of magnitude speedup compared to other conventional ways of computing the exact exchange contribution. With the efficient occ-RI-K algorithm, we were able to assess the performance of a total of 12 hybrid density functionals for computing the band gap of 25 simple solids.

From the benchmark, we found that better performing density functionals were global hybrid functionals

(B3LYP, PBE0, revPBE0, B97-3, SCAN0) where the fraction of exact exchange is between 0.20 and 0.27. A short-range hybrid functional, HSE, was found to underestimate the band gaps quite significantly compared to other hybrid functionals, consistent with a previous study.⁹ Minnesota functionals, M06-2X and MN15, are known for their good performance on main group chemistry benchmarks, but their band gaps were found to be severely overestimated due to their relatively high fraction of exact exchange. Long-range corrected density functionals (CAM-B3LYP, ω B97X-rV, ω B97M-rV, CAM-QTP01) all grossly overestimate the band gaps due to their high fraction of long-range exact exchange. We also found that the optimal fraction of long-range exact exchange in ω B97M-rV needs to vary significantly depending on materials.

Our work leaves a lot of room for future algorithmic developments, functional assessments, and functional developments. For algorithms, even with the occ-RI-K algorithm, the formal scaling of $\tilde{O}(N_k^2 N^3)$ can be too expensive for more realistic solids. By combining with tensor hypercontraction,^{82,83} one can reduce this cost to $\tilde{O}(N_k N^3)$.⁸⁴ This algorithm will enable routine application of hybrid functionals to materials that require a large k-mesh. We are currently developing and investigating this algorithm. Furthermore, an all-electron implementation of occ-RI-K will eliminate pseudopotential errors. Such an implementation will make a relative efficiency comparison possible against other all-electron exchange algorithms⁸⁵⁻⁸⁹ as well as all-electron band gap data.^{73,90,91} For functional assessments, we did not cover examples where small molecules are interacting with the surface of solids, which is commonly found in heterogeneous catalysis. We expect our combinatorially optimized density functionals to perform well for barrier heights and adsorption energies at surfaces, but there are only limited benchmark data points available.⁹² For functional developments, we noted that mid-range exact exchange functionals,⁷⁵⁻⁷⁷ functionals with system-dependent fraction of exact exchange⁷⁴ and functionals that minimize the quasiparticle correction of G0W0⁷⁹⁻⁸¹ could be worth exploring further in the future. Local hybrid functionals⁹³ and optimally tuned range-separated hybrids⁹⁴ are also good alternatives to investigate further. With the combined effort of algorithmic improvements and density functional developments and assessments, we hope to increase the predictive power and scalability of modern density functionals for simulations of molecules and materials.

VI. NOTE

Towards the completion of this manuscript, a related work on using occ-RI-K for Γ -point calculations appeared

on arXiv.⁹⁵

VII. DATA AVAILABILITY

We provide inputs for QuantumESPRESSO in the Supplementary Materials, which contains geometry information about solids studied here.

VIII. ACKNOWLEDGMENT

We thank Leo Cunha for his initial assistance with QuantumESPRESSO calculations. This work was supported by the National Institutes of Health SBIR program through Grant No. 2R44GM128480-02A1. JL thanks David Reichman for support.

IX. CONFLICT OF INTEREST

E.E. and M.H.-G. are part-owners of Q-Chem, Inc.

X. APPENDIX

A1. Numerically stable evaluation of truncated long-range Coulomb operator

In the second term in Eq. (14), we observe

$$\lim_{x \rightarrow \infty} e^{-x^2/4\omega^2} \rightarrow 0 \quad (\text{A1})$$

$$\lim_{x \rightarrow \infty} \operatorname{erf}(\omega(R_c + \frac{ix}{2\omega^2})) \rightarrow \infty \quad (\text{A2})$$

These terms cancel out giving a finite result but the individual terms quickly exceed double precision even for moderate grid sizes. The error function can be expanded about ∞ , giving:

$$\operatorname{erf}(x) = 1 - \frac{e^{-x^2}}{\sqrt{\pi}x} \sum_{n=0}^{\infty} (-1)^n \frac{(2n-1)!!}{(2x^2)^n} \approx 1 - \frac{e^{-x^2}}{\sqrt{\pi}x} \quad (\text{A3})$$

Substituting this expression into Eq. (14) cancels out the problematic terms leading to a more numerically stable form:

$$f(x) \approx \frac{4\pi}{x^2} \left[\frac{e^{-\omega^2 R_c^2}}{\sqrt{\pi}(\omega^2 R_c^2 + \mathbf{G}^2/4\omega^2)} \left(\omega R_c \cos(xR_c) - \frac{x}{2\omega} \sin(xR_c) \right) - \cos(xR_c) \operatorname{erf}(\omega R_c) \right] \quad (\text{A4})$$

* jl5653@columbia.edu

¹ Anubhav Jain, Shyue Ping Ong, Geoffroy Hautier, Wei Chen, William Davidson Richards, Stephen Dacek,

Name	B3LYP	PBE0	revPBE0	B97-3	M06-2X	MN15	SCAN0	HSE	CAM -B3LYP	ω B97X -rV	ω B97M -rV	CAM -QTP01	Exp.
C	5.98	6.09	6.13	6.39	7.85	7.29	6.26	5.32	8.22	9.54	9.25	9.86	5.48
Si	1.83	1.75	1.79	2.11	2.97	1.96	1.88	1.15	3.52	4.53	3.97	4.82	1.17
Ge	1.05	1.27	1.27	1.41	1.84	1.11	1.42	0.69	2.78	3.88	3.32	4.12	0.74
SiC	2.91	2.84	2.87	3.02	4.37	3.79	3.03	2.26	4.91	6.08	5.58	6.38	2.42
BN	6.46	6.45	6.51	6.83	8.41	7.46	6.70	5.80	8.71	10.02	9.59	10.40	6.22
BP	2.72	2.68	2.72	2.98	4.07	3.35	2.84	2.00	4.59	5.73	5.34	6.01	2.40
BAs	2.51	2.49	2.53	2.78	3.58	3.00	2.61	1.82	4.28	5.38	4.95	5.63	1.46
AlP	2.92	2.85	2.91	3.20	3.91	3.18	3.03	2.29	4.74	5.78	5.16	6.05	2.51
AlAs	2.69	2.58	2.65	2.94	3.50	2.83	2.73	2.03	4.40	5.37	4.72	5.64	2.23
AlSb	2.31	2.22	2.29	2.56	2.92	2.28	2.29	1.67	3.90	4.83	4.15	5.09	1.68
β -GaN	2.95	3.19	3.25	3.59	5.83	4.48	3.24	2.72	5.06	6.46	5.98	6.69	3.30
GaP	2.77	2.84	2.92	3.20	3.98	3.03	2.94	2.25	4.54	5.69	5.21	5.90	2.35
GaAs	1.43	1.74	1.80	1.99	3.25	1.88	1.74	1.18	3.22	4.65	4.00	4.69	1.52
GaSb	0.94	1.26	1.31	1.47	2.50	1.27	1.20	0.70	2.63	4.05	3.31	4.05	0.73
InP	1.61	1.89	1.95	2.17	3.49	2.12	1.80	1.33	3.50	4.88	4.38	4.99	1.42
ZnS	3.38	3.66	3.76	4.08	5.59	4.10	3.79	3.08	5.50	6.88	6.39	7.07	3.66
ZnSe	2.40	2.65	2.75	3.04	4.38	2.89	2.77	2.09	4.33	5.65	5.07	5.78	2.70
ZnTe	2.30	2.55	2.64	2.88	4.06	2.64	2.63	1.99	4.15	5.49	4.79	5.58	2.38
CdS	2.27	2.53	2.64	2.89	4.11	2.81	2.53	1.96	4.28	5.61	5.18	5.79	2.55
CdSe	1.60	1.83	1.94	2.18	3.27	1.94	1.82	1.29	3.44	4.70	4.21	4.84	1.90
CdTe	1.66	1.88	1.98	2.19	3.17	1.87	1.85	1.35	3.45	4.71	4.11	4.81	1.92
LiH	4.81	4.72	4.85	5.10	6.50	5.93	5.14	4.01	7.21	8.56	8.01	8.74	4.90
LiF	11.47	11.89	12.09	12.32	14.19	13.25	12.35	11.44	13.98	15.48	14.98	15.88	14.20
LiCl	8.02	8.26	8.42	8.73	9.72	8.66	8.73	7.78	10.25	11.66	11.05	11.91	9.40
AlN	6.09	6.17	6.22	6.55	8.58	7.51	6.49	5.61	8.37	9.70	9.07	10.10	6.13
RMSD	0.73	0.64	0.63	0.75	1.73	0.88	0.62	0.76	2.04	3.24	2.72	3.46	N/A
MAD	-0.01	0.12	0.19	0.45	1.63	0.61	0.26	-0.46	1.94	3.20	2.66	3.42	N/A
MAX	1.05	1.03	1.07	1.32	2.53	1.81	1.15	0.36	2.82	4.06	3.77	4.38	N/A
MIN	-2.73	-2.31	-2.11	-1.88	-0.01	-0.95	-1.85	-2.76	-0.22	1.28	0.78	1.69	N/A

TABLE AI: Experimental and theoretical band gaps (eV) from various functionals over 25 solids. The singularity treatment for exact exchange was performed via the Madelung correction. N/A means “not available”. RMSD, MAD, MAX and MIN denote, respectively, root-mean-square-deviation, mean-average-deviation, maximum signed deviation, and minimum signed deviation in reference to experimental values. All calculations were based on SCF calculations with $6 \times 6 \times 6$ \mathbf{k} -mesh.

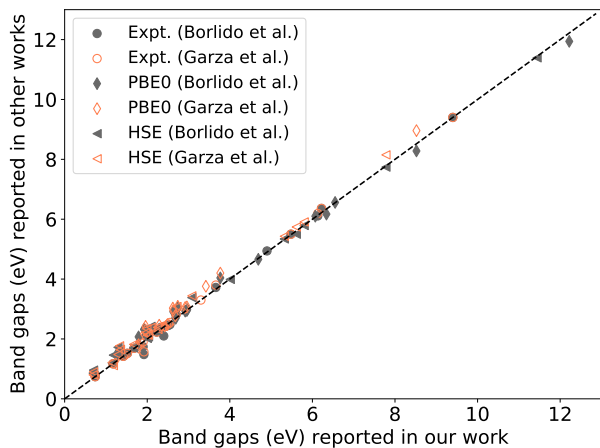


FIG. AI: Comparison among band gaps reported here, those reported in the work of Garza *et al.* (Ref. 9), and those reported in the work of Borlido *et al.* (Ref. 68.)

- Shreyas Cholia, Dan Gunter, David Skinner, Gerbrand Ceder, and Kristin A. Persson, “Commentary: The Materials Project: A materials genome approach to accelerating materials innovation,” *APL Mater.* **1**, 011002 (2013).
- Narbe Mardirossian and Martin Head-Gordon, “Thirty years of density functional theory in computational chemistry: an overview and extensive assessment of 200 density functionals,” *Mol. Phys.* **115**, 2315–2372 (2017).
 - John P. Perdew, “Density functional theory and the band gap problem,” *Int. J. Quantum Chem.* **28**, 497–523 (1985).
 - I. N. Yakovkin and P. A. Dowben, “THE PROBLEM OF THE BAND GAP IN LDA CALCULATIONS,” *Surf. Rev. Lett.* **14**, 481–487 (2007).
 - Paula Mori-Sánchez, Aron J. Cohen, and Weitao Yang, “Localization and Delocalization Errors in Density Functional Theory and Implications for Band-Gap Prediction,” *Phys. Rev. Lett.* **100**, 146401 (2008).
 - Jochen Heyd, Juan E. Peralta, Gustavo E. Scuseria, and Richard L. Martin, “Energy band gaps and lattice parameters evaluated with the Heyd-Scuseria-Ernzerhof screened hybrid functional,” *J. Chem. Phys.* **123**, 174101 (2005).
 - Yoon-Suk Kim, Kerstin Hummer, and Georg Kresse, “Accurate band structures and effective masses for InP, InAs,

Name	B3LYP	PBE0	revPBE0	B97-3	M06-2X	MN15	SCAN0	HSE	CAM -B3LYP	ω B97X -rV	ω B97M -rV	CAM -QTP01	Exp.
C	5.96	6.07	6.11	6.38	8.12	7.48	6.23	5.32	8.63	10.35	10.06	10.66	5.48
Si	1.85	1.79	1.84	2.18	3.24	2.16	1.93	1.15	3.87	5.13	4.57	5.42	1.17
Ge	1.03	1.28	1.27	1.43	2.02	1.24	1.43	0.69	3.05	4.41	3.83	4.65	0.74
SiC	3.00	2.97	3.01	3.17	4.76	4.11	3.16	2.26	5.40	6.93	6.43	7.23	2.42
BN	6.51	6.55	6.61	6.96	8.81	7.78	6.79	5.80	9.25	10.93	10.50	11.31	6.22
BP	2.70	2.69	2.73	3.02	4.33	3.55	2.85	2.00	4.96	6.40	6.01	6.68	2.40
BAs	2.50	2.49	2.53	2.80	3.81	3.18	2.61	1.82	4.62	6.00	5.57	6.25	1.46
AlP	3.00	2.96	3.02	3.33	4.23	3.44	3.14	2.29	5.14	6.49	5.87	6.77	2.51
AlAs	2.75	2.68	2.75	3.06	3.79	3.07	2.82	2.03	4.77	6.03	5.38	6.31	2.23
AlSb	2.36	2.29	2.36	2.65	3.17	2.48	2.37	1.67	4.23	5.40	4.71	5.67	1.68
β -GaN	3.12	3.42	3.48	3.85	6.40	4.93	3.46	2.72	5.75	7.54	7.06	7.78	3.30
GaP	2.81	2.92	2.99	3.29	4.27	3.24	3.01	2.25	4.91	6.31	5.83	6.52	2.35
GaAs	1.45	1.79	1.85	2.05	3.50	2.05	1.78	1.18	3.53	5.20	4.54	5.24	1.52
GaSb	0.94	1.29	1.34	1.51	2.70	1.41	1.21	0.70	2.90	4.54	3.79	4.54	0.73
InP	1.65	1.96	2.02	2.25	3.76	2.31	1.87	1.33	3.83	5.47	4.96	5.58	1.42
ZnS	3.46	3.77	3.87	4.20	5.92	4.35	3.90	3.08	5.92	7.63	7.13	7.82	3.66
ZnSe	2.46	2.74	2.84	3.15	4.68	3.11	2.86	2.09	4.70	6.33	5.75	6.46	2.70
ZnTe	2.35	2.62	2.71	2.97	4.33	2.84	2.71	1.99	4.48	6.09	5.38	6.17	2.38
CdS	2.34	2.63	2.74	3.01	4.42	3.04	2.63	1.96	4.68	6.32	5.88	6.50	2.55
CdSe	1.66	1.92	2.03	2.29	3.55	2.14	1.91	1.29	3.80	5.36	4.86	5.49	1.90
CdTe	1.71	1.96	2.06	2.28	3.42	2.05	1.92	1.35	3.76	5.29	4.68	5.38	1.92
LiH	4.78	4.69	4.81	5.06	6.44	5.87	5.11	4.01	7.14	8.69	8.10	8.88	4.90
LiF	11.73	12.22	12.42	12.68	14.91	13.83	12.68	11.44	14.85	16.82	16.32	17.23	14.20
LiCl	8.23	8.52	8.68	9.01	10.29	9.12	8.99	7.78	10.93	12.71	12.10	12.96	9.40
AlN	6.20	6.34	6.39	6.74	9.06	7.90	6.66	5.61	8.98	10.69	10.06	11.09	6.13
RMSD	0.68	0.61	0.61	0.77	2.02	1.05	0.61	0.76	2.41	3.94	3.40	4.16	N/A
MAD	0.05	0.21	0.28	0.56	1.94	0.85	0.35	-0.46	2.35	3.91	3.36	4.13	N/A
MAX	1.04	1.03	1.07	1.34	3.10	2.00	1.15	0.36	3.16	4.87	4.58	5.18	N/A
MIN	-2.46	-1.98	-1.78	-1.52	0.71	-0.37	-1.52	-2.76	0.65	2.62	2.12	3.03	N/A

TABLE AII: Same as Table AI except that this is using the truncated Coulomb scheme for the singularity correction.

and InSb using hybrid functionals,” *Phys. Rev. B* **80**, 035203 (2009).

⁸ Manish Jain, James R. Chelikowsky, and Steven G. Louie, “Reliability of Hybrid Functionals in Predicting Band Gaps,” *Phys. Rev. Lett.* **107**, 216806 (2011).

⁹ Alejandro J. Garza and Gustavo E. Scuseria, “Predicting Band Gaps with Hybrid Density Functionals,” *J. Phys. Chem. Lett.* **7**, 4165–4170 (2016).

¹⁰ Mark S. Hybertsen and Steven G. Louie, “Electron correlation in semiconductors and insulators: Band gaps and quasiparticle energies,” *Phys. Rev. B* **34**, 5390–5413 (1986).

¹¹ Lucia Reining, “The GW approximation: content, successes and limitations,” *WIREs Comput. Mol. Sci.* **8**, e1344 (2018).

¹² F. Tandetzky, J. K. Dewhurst, S. Sharma, and E. K. U. Gross, “Multiplicity of solutions to *GW*-type approximations,” *Phys. Rev. B* **92**, 115125 (2015).

¹³ Narbe Mardirossian and Martin Head-Gordon, “Mapping the genome of meta-generalized gradient approximation density functionals: The search for B97M-V,” *J. Chem. Phys.* **142**, 074111 (2015).

¹⁴ Narbe Mardirossian, Luis Ruiz Pestana, James C. Womack, Chris-Kriton Skylaris, Teresa Head-Gordon, and Martin Head-Gordon, “Use of the rVV10 Nonlocal Correlation Functional in the B97M-V Density Functional: Defin-

ing B97M-rV and Related Functionals,” *J. Phys. Chem. Lett.* **8**, 35–40 (2017).

¹⁵ Narbe Mardirossian and Martin Head-Gordon, “ ω B97X-V: A 10-parameter, range-separated hybrid, generalized gradient approximation density functional with nonlocal correlation, designed by a survival-of-the-fittest strategy,” *Phys. Chem. Chem. Phys.* **16**, 9904–9924 (2014).

¹⁶ Narbe Mardirossian and Martin Head-Gordon, “ ω B97M-V: A combinatorially optimized, range-separated hybrid, meta-GGA density functional with VV10 nonlocal correlation,” *J. Chem. Phys.* **144**, 214110 (2016).

¹⁷ L. Goerigk, A. Hansen, C. Bauer, S. Ehrlich, A. Najibi, and S. Grimme, “A look at the density functional theory zoo with the advanced GMTKN55 database for general main group thermochemistry, kinetics and noncovalent interactions,” *Phys. Chem. Chem. Phys.* **19**, 32184–32215 (2017).

¹⁸ A. Najibi and L. Goerigk, “The nonlocal kernel in van der Waals density functionals as an additive correction: An extensive analysis with special emphasis on the B97M-V and ω B97M-V approaches,” *J. Chem. Theory Comput.* **14**, 5725–5738 (2018).

¹⁹ Sebastian Dohm, Andreas Hansen, Marc Steinmetz, Stefan Grimme, and Marek P. Checinski, “Comprehensive thermochemical benchmark set of realistic closed-shell metal organic reactions,” *J. Chem. Theory Comput.* **14**, 2596–

Name	$N_k^{1/3}=1$	$N_k^{1/3}=2$	$N_k^{1/3}=3$	$N_k^{1/3}=4$	$N_k^{1/3}=5$	$N_k^{1/3}=6$	$N_k^{1/3}=7$	Q-Chem, $N_k^{1/3}=6$
C	-10.315592	-11.22904	-11.316087	-11.329812	-11.332389	-11.332836	-11.332859	-11.332728
Si	-7.263846	-7.7424678	-7.8042559	-7.8168333	-7.8200165	-7.8208858	-7.8211188	-7.820662
Ge	-7.1307138	-7.7096594	-7.7819087	-7.7978528	-7.8023892	-7.8038689	-7.8043957	-7.803826
SiC	-9.0057586	-9.5266777	-9.5911035	-9.6020953	-9.6043135	-9.6047434	-9.6047916	-9.604381
BN	-11.984863	-12.759566	-12.825463	-12.833995	-12.835224	-12.835311	-12.835242	-12.835082
BP	-8.6770283	-9.31314	-9.3866072	-9.4002713	-9.4034178	-9.4041736	-9.4043326	-9.403920
BAs	-8.3285878	-8.9973475	-9.072129	-9.0863517	-9.0897338	-9.0905892	-9.0907905	-9.090522
AlP	-8.2351585	-8.6134039	-8.6587502	-8.6664663	-8.6680014	-8.6682884	-8.6683125	-8.668096
AlAs	-7.9029732	-8.3130158	-8.3623186	-8.3712477	-8.373195	-8.3736278	-8.3737044	-8.373506
AlSb	-7.0993312	-7.507275	-7.5556889	-7.5650053	-7.5672091	-7.5677636	-7.5678933	-7.567673
β -GaN	-83.619295	-84.116855	-84.160975	-84.16707	-84.167925	-84.167964	-84.167894	-84.168307
GaP	-80.225323	-80.728226	-80.784072	-80.794673	-80.797133	-80.797732	-80.797862	-80.798163
GaAs	-79.902226	-80.432168	-80.493022	-80.505338	-80.50848	-80.509371	-80.509633	-80.509833
GaSb	N/C	-79.635938	-79.697619	-79.71142	-79.714836	-79.715891	-79.716242	-79.716115
InP	-62.105167	-62.553162	-62.598143	-62.606302	-62.608092	-62.608495	-62.608565	-62.608354
ZnS	-70.012286	-70.391394	-70.422686	-70.426918	-70.427461	-70.427451	-70.427381	-70.427359
ZnSe	-69.183122	-69.588633	-69.625613	-69.631328	-69.63231	-69.632438	-69.632414	-69.632411
ZnTe	-67.877895	-68.289422	-68.330126	-68.337139	-68.338569	-68.338851	-68.33888	-68.338818
CdS	-55.692652	-56.017378	-56.039946	-56.042664	-56.042894	-56.042816	-56.042732	-56.042425
CdSe	N/C	-55.22138	-55.249459	-55.253457	-55.254045	-55.254076	-55.254027	-55.253732
CdTe	N/C	-53.930771	-53.962107	-53.967055	-53.96794	-53.968066	-53.968049	-53.967760
LiH	-8.3559441	-8.0875882	-8.1087375	-8.1063673	-8.1064386	-8.1062722	-8.1062233	-8.106026
LiF	-31.659096	-31.869633	-31.876959	-31.87666	-31.876383	-31.876244	-31.876171	-31.875991
LiCl	-22.358903	-22.570483	-22.584203	-22.584804	-22.584638	-22.584509	-22.584435	-22.584162
AlN	-23.819271	-24.174478	-24.206023	-24.209691	-24.209945	-24.209861	-24.209777	-24.209097

TABLE AIII: B3LYP total energies per cell with varying N_k using QuantumESPRESSO with kinetic energy cutoff of 400 Ry and $N_k^{1/3} = 6$ total energies obtained from Q-Chem. N/C means not converged.

Name	$N_k^{1/3}=1$	$N_k^{1/3}=2$	$N_k^{1/3}=3$	$N_k^{1/3}=4$	$N_k^{1/3}=5$	$N_k^{1/3}=6$	$N_k^{1/3}=7$	Q-Chem, $N_k^{1/3}=6$
C	8.84	8.02	7.71	7.58	7.52	7.49	7.47	7.49
Si	4.88	4.28	4.08	4.00	3.96	3.93	3.92	3.93
Ge	2.63	1.74	1.39	1.21	1.11	1.05	1.01	1.05
SiC	8.67	8.43	8.23	8.14	8.11	8.09	8.08	8.09
BN	10.25	11.00	11.03	11.00	10.97	10.96	10.95	10.96
BP	5.96	5.33	5.10	5.00	4.95	4.93	4.92	4.93
BAs	5.65	5.05	4.83	4.73	4.68	4.66	4.65	4.66
AlP	5.55	5.11	4.93	4.85	4.81	4.79	4.78	4.79
AlAs	4.28	3.77	3.56	3.46	3.41	3.38	3.37	3.38
AlSb	3.86	3.25	3.02	2.91	2.85	2.83	2.81	2.82
β -GaN	3.04	3.35	3.28	3.21	3.17	3.14	3.12	3.14
GaP	3.81	3.36	3.15	3.04	2.98	2.95	2.93	2.95
GaAs	2.45	1.96	1.72	1.59	1.52	1.47	1.44	1.47
GaSb	N/C	0.66	0.21	1.09	1.01	0.96	0.93	0.96
InP	2.25	2.02	1.85	1.76	1.70	1.67	1.65	1.67
ZnS	3.51	3.66	3.58	3.52	3.49	3.47	3.46	3.47
ZnSe	2.65	2.72	2.61	2.54	2.50	2.47	2.46	2.47
ZnTe	2.78	2.65	2.51	2.43	2.39	2.36	2.34	2.36
CdS	2.11	2.50	2.45	2.40	2.37	2.35	2.34	2.35
CdSe	N/C	1.88	1.81	1.74	1.70	1.68	1.66	1.68
CdTe	N/C	1.97	1.86	1.79	1.75	1.73	1.71	1.73
LiH	23.58	23.54	23.47	23.47	23.47	23.47	23.47	23.47
LiF	10.29	11.74	11.78	11.76	11.75	11.74	11.74	11.74
LiCl	7.92	8.30	8.29	8.26	8.25	8.24	8.24	8.24
AlN	6.01	6.19	6.22	6.21	6.21	6.20	6.20	6.20

TABLE AIV: B3LYP band gaps at Γ based on SCF calculations with varying N_k using QuantumESPRESSO with kinetic energy cutoff of 400 Ry and $N_k^{1/3} = 6$ band gaps obtained from Q-Chem. N/C means not converged.

- 2608 (2018).
- 20 B. Chan, P. M. W. Gill, and M. Kimura, "Assessment of DFT methods for transition metals with the TMC151 compilation of data sets and comparison with accuracies for main-group chemistry," *J. Chem. Theory Comput.* **15**, 3610–3622 (2019).
 - 21 Joonho Lee, Xintian Feng, Leonardo A. Cunha, Jérôme F. Gonthier, Evgeny Epifanovsky, and Martin Head-Gordon, "Approaching the basis set limit in Gaussian-orbital-based periodic calculations with transferability: Performance of pure density functionals for simple semiconductors," *J. Chem. Phys.* **155**, 164102 (2021).
 - 22 Jianwei Sun, Adrienn Ruzsinszky, and John P Perdew, "Strongly constrained and appropriately normed semilocal density functional," *Phys. Rev. Lett.* **115**, 036402 (2015).
 - 23 Yan Zhao and Donald G. Truhlar, "A new local density functional for main-group thermochemistry, transition metal bonding, thermochemical kinetics, and noncovalent interactions," *J. Chem. Phys.* **125**, 194101 (2006).
 - 24 Haoyu S. Yu, Xiao He, and Donald G. Truhlar, "MN15-L: A New Local Exchange-Correlation Functional for Kohn–Sham Density Functional Theory with Broad Accuracy for Atoms, Molecules, and Solids," *J. Chem. Theory Comput.* **12**, 1280–1293 (2016).
 - 25 John C Slater, "A simplification of the hartree-fock method," *Phys. Rev.* **81**, 385 (1951).
 - 26 John P Perdew and Alex Zunger, "Self-interaction correction to density-functional approximations for many-electron systems," *Phys. Rev. B* **23**, 5048 (1981).
 - 27 John P Perdew, Kieron Burke, and Matthias Ernzerhof, "Generalized gradient approximation made simple," *Phys. Rev. Lett.* **77**, 3865 (1996).
 - 28 Samuel Manzer, Paul R. Horn, Narbe Mardirossian, and Martin Head-Gordon, "Fast, accurate evaluation of exact exchange: The occ-RI-K algorithm," *J. Chem. Phys.* **143**, 024113 (2015).
 - 29 Evgeny Epifanovsky, Andrew T. B. Gilbert, Xintian Feng, Joonho Lee, Yuezhi Mao, Narbe Mardirossian, Pavel Pokhilko, Alec F. White, Marc P. Coons, Adrian L. Dempwolff, Zhengting Gan, Diptarka Hait, Paul R. Horn, Leif D. Jacobson, Ilya Kaliman, Jörg Kussmann, Adrian W. Lange, Ka Un Lao, Daniel S. Levine, Jie Liu, Simon C. McKenzie, Adrian F. Morrison, Kaushik D. Nanda, Felix Plasser, Dirk R. Rehn, Marta L. Vidal, Zhi-Qiang You, Ying Zhu, Bushra Alam, Benjamin J. Albrecht, Abdulrahman Aldossary, Ethan Alguire, Josefine H. Andersen, Vishikh Athavale, Dennis Barton, Khadiza Begam, Andrew Behn, Nicole Bellonzi, Yves A. Bernard, Eric J. Berquist, Hugh G. A. Burton, Abel Carreras, Kevin Carter-Fenk, Romit Chakraborty, Alan D. Chien, Kristina D. Closser, Vale Cofer-Shabica, Saswata Dasgupta, Marc de Wergifosse, Jia Deng, Michael Diedenhofen, Hainam Do, Sebastian Ehlert, Po-Tung Fang, Shervin Fatehi, Qingguo Feng, Triet Friedhoff, James Gayvert, Qinghui Ge, Gergely Gidofalvi, Matthew Goldey, Joe Gomes, Cristina E. González-Espinoza, Sahil Gulania, Anastasia O. Gunina, Magnus W. D. Hanson-Heine, Phillip H. P. Harbach, Andreas Hauser, Michael F. Herbst, Mario Hernández Vera, Manuel Hodecker, Zachary C. Holden, Shannon Houck, Xunkun Huang, Kerwin Hui, Bang C. Huynh, Maxim Ivanov, Ádám Jász, Hyunjun Ji, Hanjie Jiang, Benjamin Kaduk, Sven Kähler, Kirill Khistyayev, Jaehoon Kim, Gergely Kis, Phil Klunzinger, Zsuzsanna Koczor-Benda, Joong Hoon Koh, Dimitri Kosenkov, Laura Koulias, Tim Kowalczyk, Caroline M. Krauter, Karl Kue, Alexander Kunitsa, Thomas Kus, István Ladjánszki, Arie Landau, Keith V. Lawler, Daniel Lefrancois, Susi Lehtola, Run R. Li, Yi-Pei Li, Jiashu Liang, Marcus Liebenthal, Hung-Hsuan Lin, You-Sheng Lin, Fenglai Liu, Kuan-Yu Liu, Matthias Loipersberger, Arne Luenser, Aaditya Manjanath, Prashant Manohar, Erum Mansoor, Sam F. Manzer, Shan-Ping Mao, Aleksandr V. Marenich, Thomas Markovich, Stephen Mason, Simon A. Maurer, Peter F. McLaughlin, Maximilian F. S. J. Menger, Jan-Michael Mewes, Stefanie A. Mewes, Pierpaolo Morgante, J. Wayne Mullinax, Katherine J. Oosterbaan, Garrette Paran, Alexander C. Paul, Suranjan K. Paul, Fabijan Pavošević, Zheng Pei, Stefan Prager, Emil I. Proynov, Ádám Rák, Eloy Ramos-Cordoba, Bhaskar Rana, Alan E. Rask, Adam Rettig, Ryan M. Richard, Fazle Rob, Elliot Rossomme, Tarek Scheele, Maximilian Scheurer, Matthias Schneider, Nikolai Sergueev, Shaama M. Sharada, Wojciech Skomorowski, David W. Small, Christopher J. Stein, Yu-Chuan Su, Eric J. Sundstrom, Zhen Tao, Jonathan Thirman, Gábor J. Tornai, Takashi Tsuchimochi, Norm M. Tubman, Srimukh Prasad Veccham, Oleg Vydrov, Jan Wenzel, Jon Witte, Atsushi Yamada, Kun Yao, Sina Yeganeh, Shane R. Yost, Alexander Zech, Igor Ying Zhang, Xing Zhang, Yu Zhang, Dmitry Zuev, Alán Aspuru-Guzik, Alexis T. Bell, Nicholas A. Besley, Ksenia B. Bravaya, Bernard R. Brooks, David Casanova, Jeng-Da Chai, Sonia Coriani, Christopher J. Cramer, György Cserey, A. Eugene DePrince, Robert A. DiStasio, Andreas Dreuw, Barry D. Dunietz, Thomas R. Furlani, William A. Goddard, Sharon Hammes-Schiffer, Teresa Head-Gordon, Warren J. Hehre, Chao-Ping Hsu, Thomas-C. Jagau, Yousung Jung, Andreas Klamt, Jing Kong, Daniel S. Lambrecht, WanZhen Liang, Nicholas J. Mayhall, C. William McCurdy, Jeffrey B. Neaton, Christian Ochsenfeld, John A. Parkhill, Roberto Peverati, Vitaly A. Rassolov, Yihan Shao, Lyudmila V. Slipchenko, Tim Stauch, Ryan P. Steele, Joseph E. Subotnik, Alex J. W. Thom, Alexandre Tkatchenko, Donald G. Truhlar, Troy Van Voorhis, Tomasz A. Wesolowski, K. Birgitta Whaley, H. Lee Woodcock, Paul M. Zimmerman, Shirin Faraji, Peter M. W. Gill, Martin Head-Gordon, John M. Herbert, and Anna I. Krylov, "Software for the frontiers of quantum chemistry: An overview of developments in the Q-Chem 5 package," *J. Chem. Phys.* **155**, 084801 (2021).
 - 30 Lin Lin, "Adaptively Compressed Exchange Operator," *J. Chem. Theory Comput.* **12**, 2242–2249 (2016).
 - 31 Gerald Lippert, Jürg Hutter, and Michele Parrinello, "A hybrid gaussian and plane wave density functional scheme," *Mol. Phys.* **92**, 477–488 (1997).
 - 32 Joost VandeVondele, Matthias Krack, Fawzi Mohamed, Michele Parrinello, Thomas Chassaing, and Jürg Hutter, "Quickstep: Fast and accurate density functional calculations using a mixed gaussian and plane waves approach," *Comput. Phys. Commun.* **167**, 103–128 (2005).
 - 33 Mirko Franchini, Pierre Herman Theodor Philipsen, Erik van Lenthe, and Lucas Visscher, "Accurate Coulomb Potentials for Periodic and Molecular Systems through Density Fitting," *J. Chem. Theory Comput.* **10**, 1994–2004 (2014).
 - 34 Qiming Sun, Timothy C. Berkelbach, James D. McClain, and Garnet Kin-Lic Chan, "Gaussian and plane-wave mixed density fitting for periodic systems," *J. Chem. Phys.* **147**, 164119 (2017).

- ³⁵ Roberto Dovesi, Fabien Pascale, Bartolomeo Civalleri, Klaus Doll, Nicholas M. Harrison, Ian Bush, Philippe D’Arco, Yves Noël, Michel Rérat, Philippe Carbonnière, Mauro Causà, Simone Salustro, Valentina Lacivita, Bernard Kirtman, Anna Maria Ferrari, Francesco Silvio Gentile, Jacopo Baima, Mauro Ferrero, Raffaella Demichelis, and Marco De La Pierre, “The CRYSTAL code, 1976–2020 and beyond, a long story,” *J. Chem. Phys.* **152**, 204111 (2020).
- ³⁶ Thomas D. Kühne, Marcella Iannuzzi, Mauro Del Ben, Vladimir V. Rybkin, Patrick Seewald, Frederick Stein, Teodoro Laino, Rustam Z. Khaliullin, Ole Schütt, Florian Schiffmann, Dorothea Golze, Jan Wilhelm, Sergey Chulkov, Mohammad Hossein Bani-Hashemian, Valéry Weber, Urban Borštnik, Mathieu Taillefumier, Alice Shoshana Jakobovits, Alfio Lazzaro, Hans Pabst, Tiziano Müller, Robert Schade, Manuel Guidon, Samuel Andermatt, Nico Holmberg, Gregory K. Schenter, Anna Hehn, Augustin Bussy, Fabian Belleflamme, Gloria Tabacchi, Andreas Glöß, Michael Lass, Iain Bethune, Christopher J. Mundy, Christian Plessl, Matt Watkins, Joost Vandevondele, Matthias Krack, and Jürg Hutter, “CP2K: An electronic structure and molecular dynamics software package - Quickstep: Efficient and accurate electronic structure calculations,” *J. Chem. Phys.* **152**, 194103 (2020).
- ³⁷ Sree Ganesh Balasubramani, Guo P. Chen, Sonia Coriani, Michael Diedenhofen, Marius S. Frank, Yannick J. Franzke, Filipp Furche, Robin Grotjahn, Michael E. Harding, Christof Hättig, Arnim Hellweg, Benjamin Helmich-Paris, Christof Holzer, Uwe Huniar, Martin Kaupp, Alireza Marefat Khah, Sarah Karbalaei Khani, Thomas Müller, Fabian Mack, Brian D. Nguyen, Shane M. Parker, Eva Perlt, Dmitriy Rappoport, Kevin Reiter, Saswata Roy, Matthias Rückert, Gunnar Schmitz, Marek Sierka, Enrico Tapavicza, David P. Tew, Christoph van Wüllen, Vamsee K. Voora, Florian Weigend, Artur Wodyński, and Jason M. Yu, “TURBOMOLE: Modular program suite for ab initio quantum-chemical and condensed-matter simulations,” *J. Chem. Phys.* **152**, 184107 (2020).
- ³⁸ Volker Blum, Mariana Rossi, Sebastian Kokott, and Matthias Scheffler, “The FHI-aims Code: All-electron, ab initio materials simulations towards the exascale,” *ArXiv* (2022), 10.48550/arXiv.2208.12335, 2208.12335.
- ³⁹ Qiming Sun, Xing Zhang, Samragni Banerjee, Peng Bao, Marc Barbry, Nick S Blunt, Nikolay A Bogdanov, George H Booth, Jia Chen, Zhi-Hao Cui, *et al.*, “Recent developments in the pyscf program package,” *J. Chem. Phys.* **153**, 024109 (2020).
- ⁴⁰ Paolo Giannozzi, Oscar Baseggio, Pietro Bonfà, Davide Brunato, Roberto Car, Ivan Carnimeo, Carlo Cavazzoni, Stefano de Gironcoli, Pietro Delugas, Fabrizio Ferrari Ruffino, Andrea Ferretti, Nicola Marzari, Iurii Timrov, Andrea Urru, and Stefano Baroni, “Quantum ESPRESSO toward the exascale,” *J. Chem. Phys.* **152**, 154105 (2020).
- ⁴¹ Jürgen Hafner, “Ab-initio simulations of materials using VASP: Density-functional theory and beyond,” *J. Comput. Chem.* **29**, 2044–2078 (2008).
- ⁴² “Welcome - FLEUR,” (2022), [Online; accessed 28. Sep. 2022].
- ⁴³ Peter Blaha, Karlheinz Schwarz, Fabien Tran, Robert Laskowski, Georg K. H. Madsen, and Laurence D. Marks, “WIEN2k: An APW+lo program for calculating the properties of solids,” *J. Chem. Phys.* **152**, 074101 (2020).
- ⁴⁴ Louisa M. Fraser, W. M. C. Foulkes, G. Rajagopal, R. J. Needs, S. D. Kenny, and A. J. Williamson, “Finite-size effects and Coulomb interactions in quantum Monte Carlo calculations for homogeneous systems with periodic boundary conditions,” *Phys. Rev. B* **53**, 1814–1832 (1996).
- ⁴⁵ James Spencer and Ali Alavi, “Efficient calculation of the exact exchange energy in periodic systems using a truncated Coulomb potential,” *Phys. Rev. B* **77**, 193110 (2008).
- ⁴⁶ Yukio Kawashima and Kimihiko Hirao, “Singularity Correction for Long-Range-Corrected Density Functional Theory with Plane-Wave Basis Sets,” *J. Phys. Chem. A* **121**, 2035–2045 (2017).
- ⁴⁷ Frank Neese and Gottfried Olbrich, “Efficient use of the resolution of the identity approximation in time-dependent density functional calculations with hybrid density functionals,” *Chem. Phys. Lett.* **362**, 170–178 (2002).
- ⁴⁸ Florian Weigend, “A fully direct RI-HF algorithm: Implementation, optimised auxiliary basis sets, demonstration of accuracy and efficiency,” *Phys. Chem. Chem. Phys.* **4**, 4285–4291 (2002).
- ⁴⁹ Hong-Zhou Ye and Timothy C. Berkelbach, “Correlation-Consistent Gaussian Basis Sets for Solids Made Simple,” *J. Chem. Theory Comput.* **18**, 1595–1606 (2022).
- ⁵⁰ Arash A. Mostofi, Jonathan R. Yates, Young-Su Lee, Ivo Souza, David Vanderbilt, and Nicola Marzari, “wannier90: A tool for obtaining maximally-localised Wannier functions,” *Comput. Phys. Commun.* **178**, 685–699 (2008).
- ⁵¹ Sylvia J. Bintrim, Timothy C. Berkelbach, and Hong-Zhou Ye, “Integral-Direct Hartree–Fock and Møller–Plesset Perturbation Theory for Periodic Systems with Density Fitting: Application to the Benzene Crystal,” *J. Chem. Theory Comput.* **18**, 5374–5381 (2022).
- ⁵² Axel D. Becke, “Density-functional thermochemistry. III. The role of exact exchange,” *J. Chem. Phys.* **98**, 5648–5652 (1993).
- ⁵³ John P. Perdew, Matthias Ernzerhof, and Kieron Burke, “Rationale for mixing exact exchange with density functional approximations,” *J. Chem. Phys.* **105**, 9982–9985 (1996).
- ⁵⁴ Yingkai Zhang and Weitao Yang, “Comment on ‘Generalized Gradient Approximation Made Simple’,” *Phys. Rev. Lett.* **80**, 890 (1998).
- ⁵⁵ Thomas W. Keal and David J. Tozer, “Semiempirical hybrid functional with improved performance in an extensive chemical assessment,” *J. Chem. Phys.* **123**, 121103 (2005).
- ⁵⁶ Yan Zhao and Donald G. Truhlar, “The M06 suite of density functionals for main group thermochemistry, thermochemical kinetics, noncovalent interactions, excited states, and transition elements: two new functionals and systematic testing of four M06-class functionals and 12 other functionals,” *Theor. Chem. Acc.* **120**, 215–241 (2008).
- ⁵⁷ Haoyu S. Yu, Xiao He, Shaohong L. Li, and Donald G. Truhlar, “MN15: A Kohn–Sham global-hybrid exchange–correlation density functional with broad accuracy for multi-reference and single-reference systems and non-covalent interactions,” *Chem. Sci.* **7**, 5032–5051 (2016).
- ⁵⁸ Kerwin Hui and Jeng-Da Chai, “SCAN-based hybrid and double-hybrid density functionals from models without fitted parameters,” *J. Chem. Phys.* **144**, 044114 (2016).
- ⁵⁹ Jochen Heyd, Gustavo E. Scuseria, and Matthias Ernzerhof, “Hybrid functionals based on a screened Coulomb potential,” *J. Chem. Phys.* **118**, 8207–8215 (2003).
- ⁶⁰ Aliaksandr V. Krukau, Oleg A. Vydrov, Artur F. Izmaylov, and Gustavo E. Scuseria, “Influence of the ex-

- change screening parameter on the performance of screened hybrid functionals,” *J. Chem. Phys.* **125**, 224106 (2006).
- ⁶¹ Jochen Heyd, Gustavo E. Scuseria, and Matthias Ernzerhof, “Erratum: “Hybrid functionals based on a screened Coulomb potential” [J. Chem. Phys. 118, 8207 (2003)],” *J. Chem. Phys.* **124**, 219906 (2006).
- ⁶² Thomas M. Henderson, Benjamin G. Janesko, and Gustavo E. Scuseria, “Generalized gradient approximation model exchange holes for range-separated hybrids,” *J. Chem. Phys.* **128**, 194105 (2008).
- ⁶³ Takeshi Yanai, David P. Tew, and Nicholas C. Handy, “A new hybrid exchange–correlation functional using the Coulomb-attenuating method (CAM-B3LYP),” *Chem. Phys. Lett.* **393**, 51–57 (2004).
- ⁶⁴ Yifan Jin and Rodney J. Bartlett, “The QTP family of consistent functionals and potentials in Kohn-Sham density functional theory,” *J. Chem. Phys.* **145**, 034107 (2016).
- ⁶⁵ Stefan Grimme, “Semiempirical GGA-type density functional constructed with a long-range dispersion correction,” *J. Comput. Chem.* **27**, 1787–1799 (2006).
- ⁶⁶ Stefan Grimme, Jens Antony, Stephan Ehrlich, and Helge Krieg, “A consistent and accurate ab initio parametrization of density functional dispersion correction (DFT-D) for the 94 elements H-Pu,” *J. Chem. Phys.* **132**, 154104 (2010).
- ⁶⁷ Stefan Grimme, Stephan Ehrlich, and Lars Goerigk, “Effect of the damping function in dispersion corrected density functional theory,” *J. Comput. Chem.* **32**, 1456–1465 (2011).
- ⁶⁸ Pedro Borlido, Thorsten Aull, Ahmad W. Huran, Fabien Tran, Miguel A. L. Marques, and Silvana Botti, “Large-Scale Benchmark of Exchange–Correlation Functionals for the Determination of Electronic Band Gaps of Solids,” *J. Chem. Theory Comput.* **15**, 5069–5079 (2019).
- ⁶⁹ S. Goedecker, M. Teter, and J. Hutter, “Separable dual-space Gaussian pseudopotentials,” *Phys. Rev. B* **54**, 1703–1710 (1996).
- ⁷⁰ C. Hartwigsen, S. Goedecker, and J. Hutter, “Relativistic separable dual-space Gaussian pseudopotentials from H to Rn,” *Phys. Rev. B* **58**, 3641–3662 (1998).
- ⁷¹ Joost VandeVondele and Jürg Hutter, “Gaussian basis sets for accurate calculations on molecular systems in gas and condensed phases,” *J. Chem. Phys.* **127**, 114105 (2007).
- ⁷² Bartolomeo Civalleri, Davide Presti, Roberto Dovesi, and Andreas Savin, “On choosing the best density functional approximation,” in *Chemical Modelling: Applications and Theory Volume 9*, Vol. 9 (The Royal Society of Chemistry, 2012) pp. 168–185.
- ⁷³ David Koller, Peter Blaha, and Fabien Tran, “Hybrid functionals for solids with an optimized Hartree–Fock mixing parameter,” *J. Phys.: Condens. Matter* **25**, 435503 (2013).
- ⁷⁴ Jonathan H. Skone, Marco Govoni, and Giulia Galli, “Self-consistent hybrid functional for condensed systems,” (2014).
- ⁷⁵ Thomas M. Henderson, Artur F. Izmaylov, Gustavo E. Scuseria, and Andreas Savin, “The importance of middle-range Hartree-Fock-type exchange for hybrid density functionals,” *J. Chem. Phys.* **127**, 221103 (2007).
- ⁷⁶ Thomas M. Henderson, Artur F. Izmaylov, Gustavo E. Scuseria, and Andreas Savin, “Assessment of a Middle-Range Hybrid Functional,” *J. Chem. Theory Comput.* **4**, 1254–1262 (2008).
- ⁷⁷ Benjamin G. Janesko, Thomas M. Henderson, and Gustavo E. Scuseria, “Screened hybrid density functionals for solid-state chemistry and physics,” *Phys. Chem. Chem. Phys.* **11**, 443–454 (2009).
- ⁷⁸ Nicholas P. Brawand, Márton Vörös, Marco Govoni, and Giulia Galli, “Generalization of Dielectric-Dependent Hybrid Functionals to Finite Systems,” *Phys. Rev. X* **6**, 041002 (2016).
- ⁷⁹ Viktor Atalla, Mina Yoon, Fabio Caruso, Patrick Rinke, and Matthias Scheffler, “Hybrid density functional theory meets quasiparticle calculations: A consistent electronic structure approach,” *Phys. Rev. B* **88**, 165122 (2013).
- ⁸⁰ Max Pinheiro, Marilia J. Caldas, Patrick Rinke, Volker Blum, and Matthias Scheffler, “Length dependence of ionization potentials of transacetylenes: Internally consistent DFT/GW approach,” *Phys. Rev. B* **92**, 195134 (2015).
- ⁸¹ Noa Marom, “Accurate description of the electronic structure of organic semiconductors by GW methods,” *J. Phys.: Condens. Matter* **29**, 103003 (2017).
- ⁸² Edward G. Hohenstein, Robert M. Parrish, and Todd J. Martínez, “Tensor hypercontraction density fitting. I. Quartic scaling second- and third-order Møller-Plesset perturbation theory,” *J. Chem. Phys.* **137**, 1085 (2012).
- ⁸³ Joonho Lee, Lin Lin, and Martin Head-Gordon, “Systematically improvable tensor hypercontraction: Interpolative separable density-fitting for molecules applied to exact exchange, second- and third-order møller-pleeset perturbation theory,” *Journal of Chemical Theory and Computation* **16**, 243–263 (2019).
- ⁸⁴ Kai Wu, Xinming Qin, Wei Hu, and Jinlong Yang, “Low-Rank Approximations Accelerated Plane-Wave Hybrid Functional Calculations with k-Point Sampling,” *J. Chem. Theory Comput.* **18**, 206–218 (2022).
- ⁸⁵ R. N. Euwema, D. L. Wilhite, and G. T. Surratt, “General Crystalline Hartree-Fock Formalism: Diamond Results,” *Phys. Rev. B* **7**, 818–831 (1973).
- ⁸⁶ I. Baraille, C. Pouchan, M. Causá, and F. Marinelli, “Comparison between Hartree-Fock and Kohn-Sham electronic and structural properties for hexagonal-close-packed magnesium,” *J. Phys.: Condens. Matter* **10**, 10969–10977 (1998).
- ⁸⁷ M. J. Gillan, D. Alfé, S. de Gironcoli, and F. R. Manby, “High-precision calculation of Hartree-Fock energy of crystals,” *J. Comput. Chem.* **29**, 2098–2106 (2008).
- ⁸⁸ Joachim Paier, Cristian V. Diaconu, Gustavo E. Scuseria, Manuel Guidon, Joost VandeVondele, and Jürg Hutter, “Accurate Hartree-Fock energy of extended systems using large Gaussian basis sets,” *Phys. Rev. B* **80**, 174114 (2009).
- ⁸⁹ Bartolomeo Civalleri, Roberto Orlando, Claudio M. Zicovich-Wilson, Carla Roetti, Victor R. Saunders, Cesare Pisani, and Roberto Dovesi, “Comment on “Accurate Hartree-Fock energy of extended systems using large Gaussian basis sets”,” *Phys. Rev. B* **81**, 106101 (2010).
- ⁹⁰ Fabien Tran and Peter Blaha, “Importance of the Kinetic Energy Density for Band Gap Calculations in Solids with Density Functional Theory,” *J. Phys. Chem. A* **121**, 3318–3325 (2017).
- ⁹¹ Fabien Tran, Sohaib Ehsan, and Peter Blaha, “Assessment of the GLLB-SC potential for solid-state properties and attempts for improvement,” *Phys. Rev. Mater.* **2**, 023802 (2018).
- ⁹² Shaama Mallikarjun Sharada, Thomas Bligaard, Alan C. Luntz, Geert-Jan Kroes, and Jens K. Nørskov, “SBH10: A Benchmark Database of Barrier Heights on Transition

- Metal Surfaces,” *J. Phys. Chem. C* **121**, 19807–19815 (2017).
- ⁹³ Toni M. Maier, Alexei V. Arbuznikov, and Martin Kaupp, “Local hybrid functionals: Theory, implementation, and performance of an emerging new tool in quantum chemistry and beyond,” *WIREs Comput. Mol. Sci.* **9**, e1378 (2019).
- ⁹⁴ Wing Dahvyd, Ohad Guy, B. Haber Jonah, R. Filip Marina, E. Gant Stephen, B. Neaton Jeffrey, and Kronik Leeor, “Band gaps of crystalline solids from Wannier-localization-based optimal tuning of a screened range-separated hybrid functional,” *Proc. Natl. Acad. Sci. U.S.A.* **118**, e2104556118 (2021).
- ⁹⁵ Sandeep Sharma, Alec F. White, and Gregory Beylkin, “Fast exchange with Gaussian basis set using robust pseudospectral method,” ArXiv.2207.04636.